Chem Soc Rev

REVIEW ARTICLE

View Article Online
View Journal | View Issue

Cite this: *Chem. Soc. Rev.*, 2024, **53**, 3606

Thermally activated structural phase transitions and processes in metal–organic frameworks

Celia Castillo-Blas, *[a] Ashleigh M. Chester,[a] David A. Keen [b] and Thomas D. Bennett [a]

Received 14th December 2023

DOI: 10.1039/d3cs01105d

rsc.li/chem-soc-rev

The structural knowledge of metal–organic frameworks is crucial to the understanding and development of new efficient materials for industrial implementation. This review classifies and discusses recent advanced literature reports on phase transitions that occur during thermal treatments on metal–organic frameworks and their characterisation. Thermally activated phase transitions and procceses are classified according to the temperaturatures at which they occur: high temperature (reversible and non-reversible) and low temperature. In addition, theoretical calculations and modelling approaches employed to better understand these structural phase transitions are also reviewed.

1. Introduction

Metal–organic frameworks (MOFs) are a relatively new class of hybrid materials which have gained great attention in the field of the materials science for more than three decades, thanks to their versatility and their interesting and modulating properties. MOFs are formed by the self-assembly of an inorganic cluster, also denoted as a secondary building unit (SBU), and an organic linker to form porous periodic networks with different topologies.[1] Owing to their remarkable porosity, MOFs have multiple desirable applications such as gas storage or separation,[2] drug delivery systems,[3] heterogeneous catalysis,[4] and sensing,[5] among others. As such, the structure–property relationship of these materials is crucial to the development of new materials for industrial implementation in these applications.

Structural phase transitions can be triggered by different stimuli such as pressure,[6] photochemical,[7] guest adsorption/desorption,[8] magnetism[9] and most importantly, temperature.[10]

Temperature is a key factor for inducing solid-state transformations in all materials and compounds. However, despite the great scope of the available literature, most studies focus only on the thermal stability of materials at high

[a] *Department of Materials Science and Metallurgy, University of Cambridge, 27 Charles Babbage Road, Cambridge, CB30FS, UK. E-mail: cc2078@cam.ac.uk*
[b] *ISIS Facility, Rutherford Appleton Laboratory, Harwell Campus, OX11 0DE, Didcot, Oxfordshire, UK*

Celia Castillo-Blas

Dr Celia Castillo-Blas obtained her PhD degree in 2019 at the Institute of Materials Science of Madrid (ICMM-CSIC) under the supervision of Dr Felipe Gándara and Prof Ángeles Monge. In 2019, she moved to Universidad Autónoma de Madrid (Spain) for a postdoctoral position working at the group of Dr Ana Platero-Prats. Currently, she is a postdoctoral research associate at the group of Prof Thomas Bennett at the University of Cambridge and her research is focused on the preparation and characterisation of MOFs-inorganic glasses composites. She has also been a visiting researcher at the University of Jena.

Ashleigh M. Chester

Ashleigh M. Chester obtained her BSc degree in Chemistry from the University of Warwick in 2018 and completed her MSc at the University of St. Andrews in 2020. She is currently a PhD student at the Department of Materials Science and Metallurgy (University of Cambridge), working on the development of novel hybrid materials comprising inorganic glasses and metal-organic frameworks (MOFs).

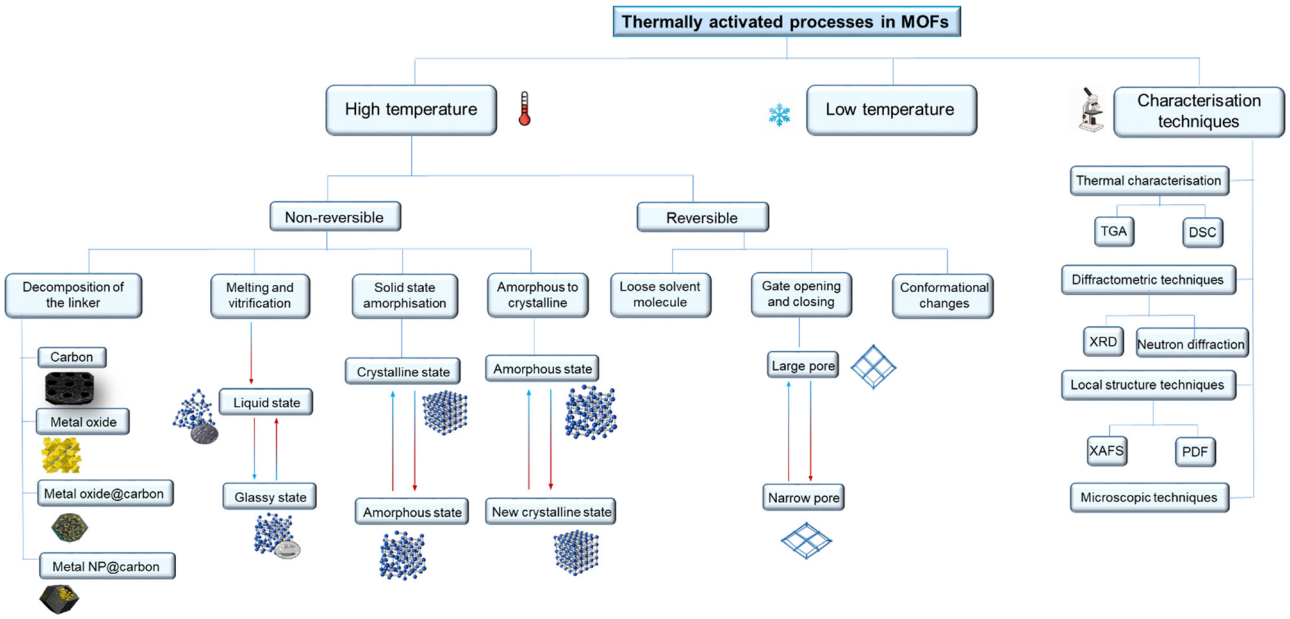

Fig. 1 Schematic representation of the potential processes and structural phase transitions that can occur by applying thermal treatment to a MOF material. They have been classified into high temperature (non-reversible or reversible) or low temperature processes and transitions. Multiple characterisation techniques to understand these phase transitions and processes are also listed.

temperatures.[11] The lack of information on temperature-induced transformations is surprising given that many MOF applications are related to a better understanding of their response at different temperatures.

Several excellent papers have reviewed the thermal stability of MOFs,[11] reversible single crystal-to-single crystal studies,[8] MOF glasses,[12,13] and MOF-derived materials obtained upon heating (carbons,[14] metal oxides, metal chalcogenides, metal carbides and metal and metal oxide composites).[15–18]

Here we review the different nature of thermally activated, structural phase transitions and processes in MOFs and classify them according to how MOFs transform under different thermal treatments (Fig. 1). Moreover, we describe in detail the characterisation techniques and approaches to theoretical calculations used to classify these transitions.

In Section 2, the review focuses on non-reversible phase transitions induced upon heating, including partial or complete decomposition of the linker, and conformational or phase changes.

David A. Keen

Professor David A. Keen was awarded his PhD at the University of Oxford in 1990, studying the structure of disordered materials by neutron scattering. He has worked on the local structure arrangements of condensed matter and has developed total scattering (pair distribution function, PDF) as well as experimental and reverse Monte Carlo computational methods to probe the relationship between structural disorder and the resulting physical properties of materials. He is currently a visiting professor at the Physics Department in Oxford University and research scientist at the ISIS Neutron Scattering Facility at the Rutherford Appleton Laboratory (Oxfordshire, UK).

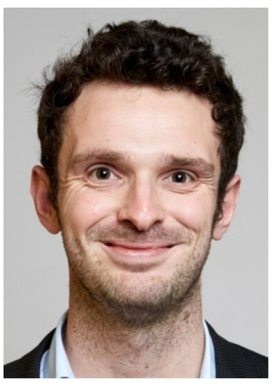

Thomas D. Bennett

Prof Thomas Bennett obtained his PhD from the University of Cambridge in 2012, working under the supervision of Professor Anthony Cheetham FRS on the physical properties of hybrid frameworks. Currently, he is an Assistant Professor at the Department of Materials Science and Metallurgy (University of Cambridge), where his group focuses on hybrid melt-quenched glasses, stimuli-responsive framework behaviour and glass-based composites. He is also currently vice-chair of the international MOF advisory committee and has been a visiting researcher at the University of Canterbury New Zeland Te Whare Wānanga o Waitaha, University of Kyoto and the Wuhan University of Technology.

Section 3 reviews the reversible structural phase transitions that occur upon heating. The phenomenon of breathing, specifically related to flexible MOFs, is described in depth. Additionally, we describe the loss and recovery of solvent molecules that induce conformational or metal-coordination environment changes.

In Section 4, we concentrate on structural changes that occur when a material is cooled; these changes are less studied but relevant as most gas uptake isotherms are recorded at low temperatures under liquid N_2 or using ice baths.

Section 5 summarises the characterisation techniques used to identify and monitor the structural phase transitions described above. These techniques include thermal characterisation, diffractometric, total scattering, microscopic and spectroscopic techniques.

Finally, Section 6 gives an account of the different theoretical calculations and modelling approaches employed to improve understanding of these structural phase transitions, as well as the thermodynamic implications to consider in these processes.

2. Non-reversible high temperature phase transitions

The thermal stability at high temperature of MOFs is often studied by thermal gravimetric analysis (TGA) as it provides information on the stability of the MOF upon heating. However, although it can reveal some phase transition temperatures, it does not provide insight on the induced structural changes and thus other techniques must be also utilised.

Depending on the conditions used during the heating process, different structural transformations may occur. The control of heating rate, dwell temperature, heating time, gas atmosphere and flow rate are crucial to obtain desired structures and to induce the desired phase transitions.

2.1. Decomposition of the linker

MOFs are sensitive materials upon heating; MOF linkers and modulators frequently decompose above the decomposition temperature (T_d) of the material, obtained from TGA. When this occurs, MOFs can form new materials with different chemical or structural characteristics in a non-reversible way, depending on the gas flow rate and the thermal treatment applied.

This approach has been widely used to prepare different MOF-derived nanostructured materials such as carbons, metal oxides, metal oxides@carbon and metal particles@carbon materials, among others (Fig. 2). These types of materials have received much interest because they are often obtained *via* the formation of hollow or hierarchical structures.[19] They are particularly suitable for electrochemical applications because MOFs have tuneable chemical compositions that can be designed at the molecular level. By judicious design of the parent MOF, advantageous properties, such as controlled porosity and high specific surface areas, can be translated to the

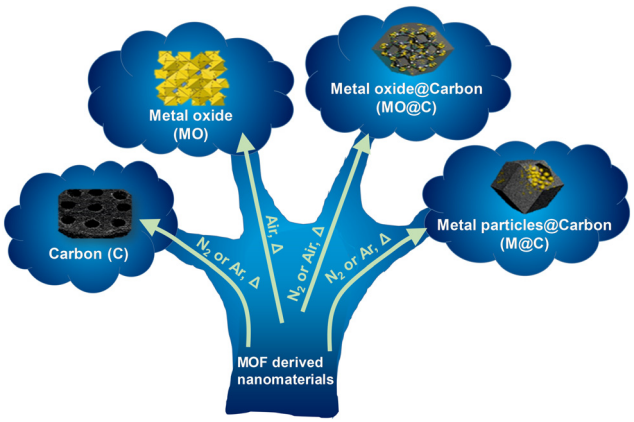

Fig. 2 Schematic depiction showing the different MOF-derived nanocomposites and materials that can be obtained upon heating.

MOF-derived material. Desired MOF-derived materials can be also obtained through a cautiously selected one-step thermal process from the parent MOF. This approach is widely applicable for their practical and industrial implementation.

2.1.1. Formation of carbons. Nanoporous carbonaceous materials have gained great attention in the materials science field thanks to their excellent thermal and chemical stability. They can be synthesised using a broad number of methodologies and resources, which makes them highly desirable. Due to their high surface areas, carbons have also been employed in the fabrication of highly efficient redox active nanostructures for energy storage. Nonetheless, materials researchers are trying to develop new synthetic approaches to design and control the porosity and morphology of nanoporous carbons. Multiple families of materials have been explored in the development of highly ordered nanoporous carbons. Therefore, MOFs are excellent candidates as precursors materials to obtain nanoporous carbons because of their intrinsic periodic porous structure. As such, these MOF-derived materials have been used in many applications including catalysis, water remediation, sensing, electrochemistry, gas storage, as capacitors or in lithium batteries.[14] Decomposition of MOFs depends on temperature, heating rate, isothermal hold temperature and gas atmosphere, amongst other factors. Tuning these parameters has resulted in different MOF-derived products, from porous carbon to metal oxides, metal sulphides, metal carbides, metal, and metal oxide decorated carbon composites.[20–22]

Carbons can be synthesised from MOFs by a thermal process of carbonisation, using different synthetic approaches, with or without post-synthetic treatment. Carbonisation is a pyrolytic exothermic reaction where the organic linker partially decomposes and graphitises; the metal nodes are reduced from metal oxides to metal nanoparticles. Despite MOF carbonisation having been monitored using multiple characterisation techniques including powder X-ray diffraction, thermal gravimetric analysis or infrared spectroscopy, it is a very complex process involving multiple reactions, and its mechanism still remains unknown. Typically, carbonisation reactions are carried out in a reducing atmosphere, using N_2, Ar, He or even H_2

as the gas flow. Depending on the temperature, as well as the metal contained in the MOF, the metal can be reduced into nanoparticles and evaporated at a high temperature (1173 K). With these conditions, the reactions involved in this process might be, but not exclusively, dehydrogenation, condensation, hydrogen transfer and isomerization for the aliphatic chains and the posterior graphitisation at higher temperatures.[52] These reactions often generate large amounts of CO_2 and H_2O gas, and they are associated with the partial decomposition of the linker and the loss of heteroatoms, as oxygen, nitrogen, hydrogen and phosphorus, among others.

The direct carbonisation of MOFs, involving just one thermal treatment step, often generates carbons with a low surface area. Usually this can be improved by a post-synthetic treatment, *e.g.* adding potassium hydroxide at high temperature and removing the potential impurities by acid washing. As a result, higher surface area carbons are obtained (>2000 m^2 g^{-1}).[53] Furthermore, the adjustment of various parameters during carbonisation, such as heating rate, the nature of the MOF linker, and carbonisation time, has also been shown to be critical in determining the properties of the resulting carbonaceous materials.

An integral part of the structure of MOFs are metal-species in their SBUs. However, these metallic species must be removed to obtain high surface area carbon materials. A promising approach using Zn-based MOFs has been well-established to efficiently produce carbonaceous materials from MOFs.[54] In this method, the MOF precursor undergoes an initial decomposition through heating in an inert atmosphere, leading to the transformation of zinc secondary building units (Zn-SBUs) into zinc oxide. Subsequently, the generated oxide is reduced to elemental zinc at 1173 K and then vaporised at this temperature, resulting in the formation of highly porous carbon material with tailored properties.

In a related example, a meticulous two-step carbonisation procedure was applied to isoreticular MOFs (IRMOFs) at temperatures of 823 K and 1173 K. This process was carefully monitored using X-ray diffraction and optical spectra (Fig. 3). Initially, the IRMOFs underwent transformation into a MOF-carbon composite at a relatively lower temperature (<1023 K), marked by the degradation of the primary MOF structure. Subsequently, as the temperature increased, a transition to a pure carbonaceous material occurred at 1173 K. During this transformation, zinc species originally present as ZnO were reduced to elemental zinc, which was subsequently vaporised. This series of reactions resulted in the production of a pure carbonaceous product, boasting an impressive surface area of 3447 m^2 g^{-1}.[37]

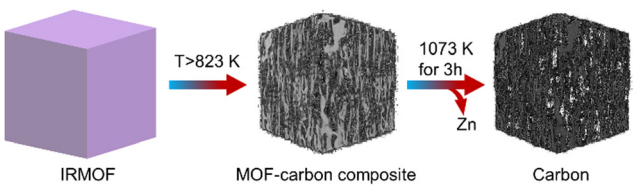

Fig. 3 Schematic depiction of the structural changes of IRMOF-1 with heat treatment to yield MDC-1.[37]

Alternatively, when a lower carbonisation temperature is applied, metals are retained in the carbonised samples. This also occurs in MOFs with SBUs consisting of metals with higher boiling points, such as iron, cobalt, copper or nickel. Conversely, these MOFs generate very porous carbon products after a post-acid wash treatment.[55]

In addition, the dimensionality of the MOF precursor can be retained in the final carbon products, culminating in possible materials with dimensionality ranging from zero-dimensional (0D) to three-dimensional (3D). An example of a 0D carbon material was prepared from ZIF-8 nanoparticles. These particles were heated to 773 K, producing carbon nanodots with an average particle size of 2.2 nm.[24] Carbonaceous one-dimensional (1D) materials, such as carbon nanotubes, can also be obtained from MOFs with metal species such as Fe, Co, and Ni.[56] In the high-temperature treatment, metallic nanoparticles were initially formed. Then, they catalysed the growth of carbon nanotubes on their surfaces.[57] One such example was the pyrolysis without the addition of a catalyst or carrier gas at 773 K for 20 hours of $[Ni_3(BTC)_2]\cdot 12H_2O$ (BTC = benzene-1,3,5-tricarboxylate) in a tube furnace, which resulted in multi-walled carbon nanotubes (MWCNT).[51] Utilising a different approach, two-dimensional (2D) carbon materials can also be synthesised from MOFs.[58] For instance, a notable example involved the production of graphene-like carbon nanosheets by subjecting a composite of ZIF-7 and glucose to a carbonisation process in an Ar atmosphere at a temperature of 1223 K for five hours.[42] ZIFs, zeolitic imidazolate frameworks, are a subclass of MOFs composed of divalent metal cation in a tetrahedral coordination environment linked through imidazolate ligands. Another example described the synthesis of a N-doped graphene particle analogue with a high nitrogen content (17.72%) from the pyrolysis of ZIF-8 particles for lithium storage applications.[59] 2D carbon nanosheets have been also prepared from an Al-MOF for use in Li–Se batteries.[49] These examples demonstrate the structural versatility of MOF-derived carbon products; several additional examples of carbon-derived materials from MOFs are also summarised in Table 1. The thermal treatment used to prepare them, as well as their applications, are also given.

Hollow carbon structures can also be produced from MOFs. The external-templating approach is conducted to create these materials with superior surface areas and loading capacities. This consists of coating a sacrificial or removable template, such as silica or polystyrene, with the desired MOF. In an example reported in 2014, hollow porous carbon (HPC) spheres were prepared by the pyrolysis of polystyrene@ZIF-8 core–shell microspheres.[50]

2.1.2. Formation of metal oxides. Amongst the numerous methods for producing metal oxides, one notable approach gaining prominence involves subjecting MOFs to thermal treatments. This method offers an alternative and promising pathway for crafting metal oxides with precisely engineered nanostructures and compositions to suit specific applications.[60] This is an effective and facile way to prepare

Table 1 Representative examples of carbon materials using sacrificial MOFs as templates and their thermal treatment conditions and applications. (S-PC = porous carbon containing sulphur)

MOF precursor	Product	Thermal treatment	Application	Ref.
ZIF-8	NPC	1173 K, N_2	ORR	23
ZIF-8	CND-0D	773 K, N_2		24
ZIF-8	N-PC	1073 K, N_2	Sensing	25
ZIF-8	NPC	673 K, N_2	Adsorption of ethopabate	26
ZIF-8, sulfur powder	S-PC	1323 K, NH_3	Lithium–sulphur batteries	27
ZIF-8	N-PC	973 K, N_2	Cancer therapy	28
ZIF-8, melamine	N-PC	1223 K, N_2	Catalysis	29
ZIF-8	PC	1173 K, N_2	Batteries	30
ZIF-8	N-PC	1273 K, N_2	Water remediation	31
Zn-MOF	PC	1173 K, Ar	Supercapacitor	32
Zn-MOF	PC	1073 K, N_2	Energy storage	33
MOF-5	PC	1273 K, Ar	Water remediation	34
MOF-5	PC	N_2	Catalysis	35
MOF-5	PC	1173 K	Capacitor	36
MOF-5	PC	1073 K, Ar	Gas storage	37
MOF-5	PC	823 K	Lithium batteries	38
MOF-74 (Zn/Fe)	PC	1273 K, N_2	Water remediation	39
MOF-74 (Mg)	PC	923 K, N_2	Capacitive deonisation	40
Mg-MOF	PC	973 K, N_2	Capacitive deonisation	41
ZIF-7, glucose	NPC	1223 K (5 h), Ar		42
Zn-MOF	PC-2D	1173 K, Ar	Supercapacitor	43
ZIF-67	PC	1073 K, Inert gas	Capacitor	44
MIL-88 (Fe)	PC	1173 K, N_2	Capacitive deonisation	45
MIL-53(Fe)	PC	1073 K, N_2	Water remediation	46
PCN-224, 222	N-PC	1273 K, N_2	CO_2 reduction	47
UiO-66	PC	1073 K, N_2	Catalysis	48
Al-MOF	PC-2D	1073 K, Ar	Batteries	49
ZIF-8	HPC	1273 K, N_2		50
$Ni_3(BTC)_2$	MWCNT			51

desired metal and mixed metal oxides from MOFs by controlling two parameters, atmosphere and temperature. Typically, metal oxides with higher oxidation numbers are obtained after calcination of MOFs in air, whilst metal oxides with lower oxidation numbers are obtained after pyrolysis, usually under N_2 atmosphere. The resulting nanoporous oxide materials usually retain the shape and partial porosity of the parent MOFs, which are favourable for obtaining larger surface areas than the oxides prepared following other methodologies.

These MOF-derived metal oxides have been widely studied in different electrochemical applications such as lithium–air batteries,[21,61–63] oxygen reduction reaction (ORR), carbon dioxide reduction, supercapacitors, water splitting,[64] and others. They are also used as catalysts.

The structure of the resulting oxide is intricately shaped by a combination of factors, including the original composition of the MOF, the specific temperature and the duration of the thermal treatment applied. For MOF precursors containing cobalt, manganese, or iron, the calcination process often forms spinel oxides as the prevailing outcome. However, non-spinel oxides, such as CoO, Fe_2O_3, and Mn_2O_3 can be also obtained by controlling temperature, gas flow, time heated and heating rate. Other examples indicate the calcination of Zn, Cu, Ni and Ti-based MOFs leads to MgO, ZnO, CuO, NiO, TiO_2 and ZrO_2 as the products.

To date, a great number of porous metal oxide nanomaterials have been derived from MOF precursors, including cupric oxide (CuO),[65] cobalt oxide (Co_3O_4),[66] iron oxide (Fe_2O_3),[67] magnesium oxide (MgO),[68] manganese oxide (Mn_2O_3),[69] nickel oxide (NiO),[70] titanium dioxide (TiO_2),[71] and zinc oxide (ZnO).[72] This approach has also been expanded to mixed transition metal oxides, such as ferrites ($CoFe_2O_4$ and $Mn_{1.8}Fe_{1.2}O_4$),[73] cobaltites ($ZnCo_2O_4$, $Zn_xCo_{3-x}O_4$) and manganites ($ZnMn_2O_4$), including four-metal oxides with the spinel structure ($Zn_{3-x-y-z}Mn_xCo_yCa_zO_4$). These have been employed for the ORR and reverse water–gas shift reaction (carbon dioxide reduction).[74,75] Several representative examples are summarised in Table 2, where the MOF precursor, thermal treatment and applications are listed.

During the process of synthesising metal oxides, meticulous control of various parameters holds significant importance. These include factors such as surface area, chemical composition, particle size and shape, as well as the oxidation state. A recent example showcased the control of composition using MOF-derived methods, where nanoplate assemblies of $ZnMn_2O_4$ from a bimetallic MOF, $ZnMn_2$–ptcda (ptcda = perylene-3,4,9,10-tetracarboxylic dianhydride) were created through heat treatment.[80] Temperature control was critical for obtaining the desired spinel oxide. Additionally, a mixed valence metal oxide hollow structure (CuO/CuO_2) has been synthesised by thermolysis at 523 K from $[Cu_3(BTC)_2]_n$.

In another example, Co_3O_4 particles, with a size of about 25 nm, but a low surface area of 5.3 $m^2\ g^{-1}$, were obtained from a Co-MOF.[79] A method for selectively converting MIL-88B (Materials from the Lavoisier Institute) into either Fe_2O_3 or Fe_3O_4 has been demonstrated. When MIL-88B is heated in the

Table 2 Representative examples of metal oxides obtained using MOFs as sacrificial templates. Thermal treatment conditions and their applications are also summarised

MOF precursor	Metal oxide	Thermal treatment	Application	Ref.
MOF-199	CuO	Air, 723 K, 2 h	Capacitor	65
Mg-*aph*-MOF	MgO	Air, 773 K, 12 h	CO_2 uptake	68
Mn-BTC	Mn_2O_3	Air, 723 K, 2 h	Li-battery	69
Fe-MIL-88B	Fe_2O_3	Air, 657 K	Magnetic material	76
Fe-MIL-88B	Fe_3O_4	N_2 973 K	Magnetic material	76
Ni-BTC	NiO	Air, 973 K, 1 h	Li-battery	77
Ni-BTA	NiO	Air, 773 K, 2 h	Li-battery	70
Co-BDC	Co_3O_4	Air, 723 K, 2 h	Supercapacitor	78
$(Co_3(NDC)_3(DMF)_4)$	Co_3O_4	Air, 873 K, 1 h	Li-battery	79
MIL-125 (Ti)	TiO_2	Air, 673 K, 4 h	Li-battery	71
$ZnMn_2$–ptcda	$ZnMn_2O_4$	Air, 723 K, 1 h		80
Ni–Fe–PB	$NiFe_2O_4$	Air, 973 K, 6 h	Li-battery	81
Ni/Fe MIL-88	$Ni_{0.62}Fe_{2.38}O_4$	Air, 773 K	Li-battery	82
ZIF-67	$Ni_xCo_{3-x}O_4$	Air, 623 K, 1.5 h	OER	83
$Zn_{1-x-y-z}Mn_xCo_yCa_z$(hfipbb)	$Zn_{3-x-y-z}Mn_xCo_yCa_zO_4$	1073 K, 24 h	ORR, CO_2 reduction	74,75
ZIF-67	Hollow Co_3O_4	533 K, air, 3 h	OER	84
$[Cu_3(btc)_2]_n$	Cu_2O/CuO	Air, 623 K	Li-battery	85
Fe_2Ni MIL-88/Fe MIL-88	$NiFe_2O_4/Fe_2O_3$	Air, 723 K, 6 h	Li-battery	86
ZIF-67@NiCoLDH	$Co_3O_4/NiCo_2O_4$	623 K, 2 h	OER, CO_2 methanation	87
$Co_3[Fe(CN)_6]_2$@$Ni_3[Co(CN)_6]_2$	Fe_2O_3@$NiCo_2O_4$	Air, 723 K, 6 h	Li-battery	88,89

presence of air, it transforms directly into hematite (Fe_2O_3). However, employing a two-step process involving calcination followed by heating in an inert atmosphere yields magnetite (Fe_3O_4). By using MIL-88(Fe) as a sacrificial template, spindle-like mesoporous Fe_2O_3 structures with a surface area of 75 m^2 g^{-1} were produced. This approach involved a two-step thermolysis, which included heating in a N_2 environment, followed by calcination in air.[76]

Many MOFs have been designed with core–shell structures for different uses, but creating core–shell metal oxide nanostructures from MOFs has proven more challenging. These challenges notwithstanding, derived core–shell metal oxides have gained increasing attention because of their excellent electrochemical performance and catalytic properties as they combine the electrochemical properties of both oxides. As an illustrative example, a two-step methodology has been employed to fabricate Co_3O_4@$NiCo_2O_4$ double-shelled nanocages, featuring distinct shell compositions. This innovative approach employs MOF particles as precursors. In this work, ZIF-67 particles were dispersed within a $Ni(NO_3)_2$ solution, giving rise to the formation of ZIF@Ni–Co yolk-shelled structures (Fig. 4).[87] A subsequent annealing treatment converted the ZIF-67 cores and Ni–Co shells into Co_3O_4 (inner core) and $NiCo_2O_4$ (external shell), respectively. Another representative example is the thermal conversion of $Co_3[Fe(CN)_6]_2$@$Ni_3[Co(CN)_6]_2$ nanotubes to porous Fe_2O_3@$NiCo_2O_4$ nanocages as anode materials for Li-batteries.[88]

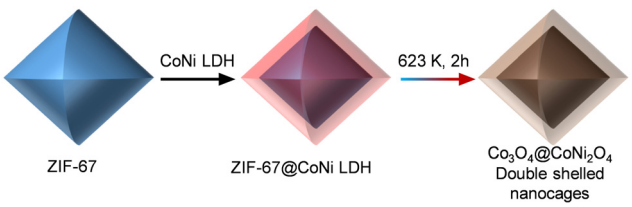

Fig. 4 Schematic illustration of the formation process of Co_3O_4@$NiCo_2O_4$ double-shelled nanocages.[87]

Hollow metal oxide polyhedra can be also obtained using the external-templating approach. For this approach, a core–shell structure with ZIF-67 over micelles was prepared with a surfactant, alkyltrimethylammonium bromide (C_nTAB; n = 12, 14 or 16), in aqueous media and calcined at 533 K for three hours.[84]

2.1.3. Formation of metal/metal compound composites. As previously mentioned, metal oxides are useful in various electrochemical energy storage and conversion applications that require a large surface area. Therefore, scientists are exploring new ways to create metal oxide-carbon (MO@C) composites.[90,91]

Traditional synthetic approaches of MO@C composites often lead to poor control over the metal oxide particle sizes because of agglomeration, which alters their electrode material performance. However, researchers can optimise thermolysis by heating MOFs, resulting in highly porous composites, MO@C and M@C (metal nanoparticles decorated carbon composites), because of the high surface area carbon produced in the process. This in turn mitigates particle agglomeration.

In one example, hybrid Co_3O_4@C porous nanowire arrays were prepared from a Co-naphthalenedicarboxylate MOF precursor with a layered crystalline structure. They were directly grown on copper foil using a low-temperature (353 K) hydrothermal process. Then, the components in the MOF were transformed into Co_3O_4 and carbon through carbonisation in a nitrogen atmosphere. This process produced nanowires with internal pores (Fig. 5). The resulting material had a high surface area of 251 m^2 g^{-1} and a substantial carbon content of 52.1 wt%.[92]

A key study about the limits on obtaining metal, metal oxides and mixed metal–metal oxides particles concluded that the reduction potential of the coordination metal plays a

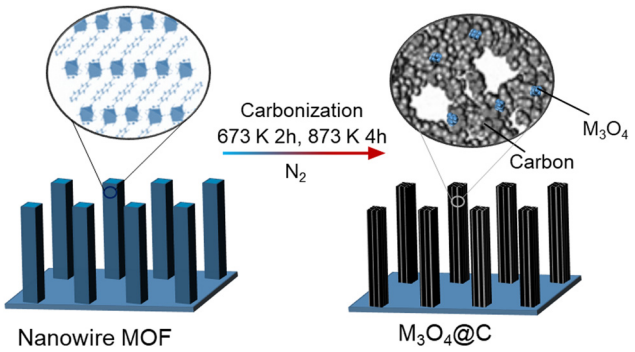

Fig. 5 Schematic illustration for the fabrication of M_3O_4–C nanowire arrays.[92] Inspired from ref. 92.

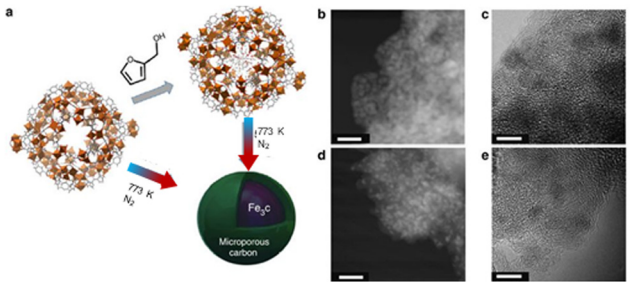

Fig. 6 (a) MOF mediated synthesis strategy for the Basolite F-300 material. (b) High-angle annular dark-field scanning electron (HAADF STEM) images of Fe@C (scale bar, 20 nm). (c) High-resolution (HRTEM) micrographs of 38-Fe@C (scale bar, 5 nm). (d) HAADF STEM of 25-Fe@C (scale bar, 20 nm) HRTEM image of 25-Fe@C (scale bar, 5 nm). Adapted from ref. 95 with permission from Springer Nature, copyright 2015.

critical role in determining the resultant product. The decarbonisation process generated metallic species through thermolysis when the reduction potential surpassed −0.27 V. However, at lower reduction potential values than −0.27 V, thermolysis produced a metal oxide as the resulting product.[93] The study involved several MOFS, such as MOF-4, HKUST-1, Zn-ADA-1, MnHFMOF-D, MOF-CJ4, Cd-MOF-1, *etc.*

2.1.4. Formation of metal nanoparticles@carbons. Metal nanoparticles embedded in a porous carbonaceous matrix are very desirable materials for heterogeneous catalysis and various other applications.[16] Traditional approaches, as mentioned above, of dispersing metal nanoparticles into a carbon matrix often result in agglomeration of the nanoparticles, decreasing their efficacy as catalysts.

A MOF pyrolysis approach to prepare NP@C (carbon embedded nanoparticles) materials has also gained attention. Cobalt-based MOFs have been widely explored using this methodology to obtain Co@C–N (carbon–nitrogen embedded cobalt nanoparticles) and Co@C (carbon embedded cobalt nanoparticles) (Table 3).[94]

Gascon *et al.* demonstrated an innovative approach, exemplifying excellent dispersion of iron nano-particles within a porous carbon matrix.[95] This methodology involved the impregnation of the Fe-precursor (Basolite F-300) with a carbon source, followed by pyrolysis, as illustrated in Fig. 6.

Hollow M@carbon composites can be also prepared using a similar thermal treatment. These hollow materials have larger surface areas, superior loading capacities and lower densities than their counterparts. This makes them highly desirable materials for electrochemical and catalytic applications.

2.2. Melting and vitrification behaviour

Traditionally, the MOF field has focused almost entirely on the crystalline domain. However, order–disorder and solid–liquid-glass phase transitions upon heating are commonly observed and the resulting phases have great importance in materials science.[105] Some of their properties are beneficial for material processing and provide unique features for their industrial implementation.[106,107]

The solid to liquid transition is reached upon heating above the melting point of the material. This transformation is reversible and the mechanism can be explained for simple systems following the Lindemann criterion, which proposes that melting occurs when the root-square of the vibration amplitude of particles in crystals exceeds a critical threshold proportion of the interparticle distance.[108,109] It is also crucial that the material possesses a decomposition temperature (T_d) higher than the melting temperature (T_m), to avoid the total or partial decomposition of the material during melting. These temperatures vary according to the nature of the solid material (covalent, organic, inorganic), the applied pressure and the surrounding environment (argon, air, nitrogen, *etc*).[110] These criteria mean that melting has rarely been observed because of

Table 3 Representative cases of metal and metal nanoparticles carbon derived composites and their thermal treatment conditions and applications, using a MOF as a sacrificial template

MOF precursor	M@C/M@C–N	Thermal treatment	Application	Ref.
ZIF-67	Co@C–N	1073 K, 8 h, Ar	Oxidation of alcohols to esters	94
ZIF-67	Co@C–N	873–1173 K, 10 h, Ar	Catalysis	96
ZIF-67	Co–CoO@C–N	773–1073 K, 3 h, under N_2	Nitroarene hydrogenation	97,98
ZIF-67	Co@CN	1173 K, 2 h, N_2	ORR	99
$Co_9(btc)_6(tpt)_2(H_2O)_{15}$	Co@C–N	Ar 20 mL min^{-1}, 773–1173 K	Oxydative amidation of aldehydes	100
$Co[(1,4\text{-bdc})(ted)_{0.5}]\cdot 2DMF\cdot 0.2\,H_2O$	Co@C–N	773–1073 K 8–15 h, Ar	Hydrogenation of aliphatic and aromatic	101
ZIF-8	Zn@C–N	973–1073 K, 2 h, heating rate 5 K min^{-1}, N_2 60 mL min^{-1}	CO_2 cycloaddition with epoxides	102
MUV-3: $[Fe(mIm)_2]$	Fe@C	973 K, 3.5 h, under N_2	OER	103
Basolite F-300	Fe@C	773 K 8 h N_2	Fischer–Tropsch catalysis	95
Fe/Co-MOF	Fe/CoO_x@C	973–1173, 0.5 h,	OER	104

the relatively low thermal stability of the MOF and coordination polymer (CP) materials.[11]

Different families of hybrid materials, such as hybrid-organic inorganic perovskites (HOIPs), CPs and porous organic cages (POCs) have shown melting upon heating. Usually, these materials have melting temperatures around 400–500 K.[111] For example, dicyanamide-based HOIPs and their derivatives melt at 379–535 K.[112] This melting temperature can easily be varied by changing the ammonium cation located at the perovskite A sites, as well as the B site metal cation.

Despite the reduction of intrinsic porosity of the crystalline MOF after a liquid phase transition, opportunities have been identified for the unique behaviour of dense and processable melt-quenched glass phases. Glassy MOFs are mouldable and grain boundary-free, both properties may facilitate the fabrication of homogeneous membranes for gas separation, solid electrolytes, optical materials and composite hybrids. However, until now, examples of porous 2D and 3D CPs or MOFs that melt remains scarce.

However, glassy MOFs can be synthesised using other routes including mechanical vitrification[113] or direct synthesis.[114,115] These avoid the issues associated with the thermal decomposition of MOFs, but the most conventional route to glassy MOFs formation remains melt-quenching.[13]

From a molecular-kinetics point of view, the equilibrium liquid to non-crystalline solid transition may be considered as a fourth order phase transition, different to gas, liquid and solid states.[116] A melt-quenched glass, also known as a 'frozen-liquid', is a disordered material that lacks the periodicity of crystals, but behaves mechanically like solids. They are formed by cooling a liquid fast enough to avoid crystallisation (Fig. 7).[117] They can be distinguished from other amorphous solids by the presence of a glass transition temperature (T_g). T_g is a temperature or temperature range over which a reversible transition between a glassy state and a more viscoelastic state occurs.

The first MOF which demonstrated the ability to melt and form a glass after quenching was ZIF-4.[118] ZIF-4, $Zn(Im)_2$ (Im^- = imidazolate), is a material with a **cag** network topology possessing one of the most complex behaviours upon heating in MOF-based materials.[119] ZIF-4 amorphises at 603 K before recrystallising into a denser phase denoted ZIF-**zni** at 673 K.[120] This denser ZIF-**zni** phase melts at 863 K, and then decomposes at a slightly higher temperature (873 K).[121] The melted liquid can be quenched by rapid cooling down before decomposition occurs, producing a ZIF glass with a T_g of 565 K.[118] However, the melting point of ZIF-**zni** is very high and exhaustive efforts have been explored to minimise this T_m value, whilst maintaining the porosity of the ZIF-4 structure and preventing decomposition of the material upon heating. The addition of other linkers into the ZIF-**zni** structure drastically changes the thermal behaviour of its structure. ZIF-61, $[Zn(Im)_{1.35}(mIm)_{0.65}]$ (mIm = 2-methylimidazolate), decomposes upon heating without passing through the liquid state. On the other hand, trace amounts of 5-aminobenzimidazolate (abIm) into the ZIF-**zni** structure creates a new material, $[Zn(Im)_{1.995}(abIm)_{0.005}]$, which melts at 842 K (a lower temperature than that of pristine ZIF-4 **zni**) with no evidence of decomposition to zinc oxide.[122]

The most well-known approach for reducing T_m is partial substitution of the imidazolate ligand by another imidazole-derived linker, such as benzylimidazolate (bIm^-) in the structure. This led to the idea of exploring the thermal behaviour of ZIF-62, $[Zn(Im)_{2-x}(bIm)_x]$ (Im^- = imidazolate, x = 0.1–0.3). It was found that the T_gs of ZIF-62 (in the range of 571–593 K) can be tuned by changing the Im/bIm ratio.[123] Isostructural ZIF analogues with **cag** topology have also been prepared with cobalt, which exhibit even lower T_g values (533–563 K). Additionally, multivariate-MOFs (MTV-MOFs) have T_gs which can be modified using mixtures of different linkers and metals.[124]

Moreover, the addition of other benzylimidazolate linkers with different functionalities has also been explored to investigate their thermal behaviour, improve their mechanical performance and add new properties. For example, by adding 2-aminobenzylimidazole as a linker, an amino functionality was introduced to create a new ZIF, ZIF-UC-6, with T_g and T_m values of 589 and 618 K, respectively.[125] Interestingly, the surface of this glass can be post-synthetically modified, which changes its hydrophobicity. In a different example, the substitution of benzylimidazolate with purinate (pur^-) in the ZIF-62 structure led to increased CO_2 uptake capacity for both the resulting crystalline and glass ZIF-UC-7, $Zn(Im)_{1.75}(pur)_{0.25}$.[126]

Recently, imidazole was substituted in ZIF-4 by an imidazole containing cyano groups, forming ZIF-4-CNx materials, with the following compositions: $[Zn(Im)_{2-x}(CNIm)_x]$ $CNIm^-$ = 4-cyanoimidazolate, ($0.04 \leq x \leq 0.39$) and $[Zn(Im)_{2-x}(dCNIm)_x]$, $dCNIm^-$ = 4,5-dicyanoimidazolate, ($0.10 \leq x \leq 0.28$).[127] This family of materials melts and forms melt-quenched glasses with a range of T_gs between 527 K and 249 K that can be easily varied controlling the Im/CNIm ratio.

Apart from Zn and Co, other metals can also be investigated. Recently, a very interesting iron non-porous CP $[Fe_3(Im)_6(Him)_2]$[128] was studied upon heating. This CP exhibits a mass loss associated with the removal of the terminal imidazoles under N_2 atmosphere over 556 K. This mass loss is associated with a structural phase transition to a crystalline phase denoted MUV-24 $[Fe(Im)_2]$ with a **lla** topology.[129] Further heating under N_2 flow results in another structural transition to form a **zni** polymorph above 690 K. This polymorph is able to melt above 755 K and form a melt-quenched glass after rapid cooling. Additionally, changing the conditions upon heating produces

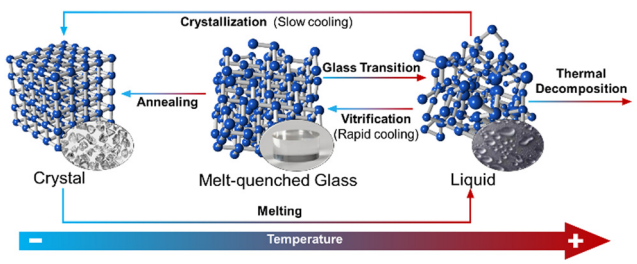

Fig. 7 Schematic depiction of the processes for achieving melt-quenched CP/MOF glasses.

Table 4 List of published melted-quenched MOF and 3D CP glasses and information about their melting and glass transition temperature

MOF/CP precursor	T_m/K	T_g/K	Ref.
ZIF-zni: $[Zn(Im)_2]$	836	565	118,121
ZIF-4-CN$_x$: $[Zn(Im)_{2-x}(CNIm)_x]$ (x = 0.04–0.39)		549–543	127
ZIF-4-dCN$_x$: $Zn(Im)_{2-x}(dCNim)_x$ (x = 0.10–0.28)		545–527	127
ZIF-62: $[Zn(Im)_{2-x}(bIm)_x]$ (x = 0.05–0.35)	645–714	571–593	121,123,145
ZIF-62 (Co): $[Co(Im)_{2-x}(bIm)_x]$ (x = 0.10–0.30)	659–705	533–263	121,145
$[Co_{0.2}Zn_{0.8}(Im)_{1.95}(bIm)_{0.025}(5\text{-ClbIm})_{0.025}]$	583	561	146
ZIF-UC-1: $[Zn(Im)_{2-x-y}(bIm)_x(mbIm)_y]$	691–706	578–589	124
ZIF-UC-2: $[Zn(Im)_{1.90}(6\text{-Cl-}5\text{-FbIm})_{0.10}]$	679	523	147
ZIF-UC-3: $[Zn(Im)_{1.75}(5\text{-Cl-}2\text{-mbIm})_{0.25}]$	663	609	147
ZIF-UC-4: $[Zn(Im)_{1.63}(5\text{-FbIm})_{0.37}]$	694	563	147
ZIF-UC-5: $[Zn(Im)_{1.69}(5\text{-ClbIm})_{0.31}]$	705	593	147
ZIF-UC-6: $[Zn(Im)_{1.82}(abIm)_{0.18}]$	618	589	125
ZIF-UC-7: $[Zn(Im)_{1.75}(pur)_{0.25}]$	591	546	126
TIF-4: $[Zn(Im)_{1.5}(mbIm)_{0.5}]$	713	623	121
ZIF-zni-NH$_2$: $[Zn(Im)_{1.995}(abIm)_{0.005}]$	842	616	122
MUV-24: $[Fe(Im)_2]$	755	463	129
$[M(L1)_2]$ (M = Zn, Co, Mn, Cd)	NA	421–504	130
$[M(L1X)_2]$ (L2X = L2, L2F, L2Cl, L2Br, L1NH$_2$)	NA	393–562	130
$[Co(L3)_2]$	NA	498	130
$[Co(L4)_2]$	NA	553	130
$[Co(L5)_2]$	NA	526	130
$[Co(L6)_2]$	NA	529	130
[Co(byp)]fum	NA	396	131
[Co(byp)]bdc	NA	393	131
[Co(bpee)]bdc	NA	393	131
$[Ag(pL2)(CF_3SO_3)]\cdot 2C_6H_6$	544	434	148
$[Ag(mL1)(CF_3SO_3)]\cdot 2C_6H_6$	442	341	148
$[Cu_2(SCN)_3(C2bpy)]$	460	341	149
$[Cu_2(SCN)_3(C4bpy)]$	411	332	149
$[Cu_8(SCN)_{12}(Phbpy)_4]$	490	344	149
$[Cu(SCN)_2(3\text{-Pybpy})]$	476	345	149

another phase transition from MUV-24 (**lla**) to MUV-24 with a **coi** topology.

Although the ZIF family encompasses the most representative examples of melting materials, other coordination polymers (CPs) with different dimensionalities can also melt, where several can form a glass without recrystallisation upon rapid cooling down (Table 4).

Most meltable CPs and MOFs contain imidazolate and triazolate linkers combined with metal cations of the first transition series, most of them containing Zn^{2+}. Very recently, Horike *et al.* have observed for the first time the vitrification phase transition of a coordination polymer containing carboxylate linkers *via* the decoordination of the water molecules from the network structure before recrystallisation to porous glasses.[130] This has also been demonstrated in coordination polymers containing terephthalate linkers.[131] These unprecedented results promise new and exciting avenues to obtain hybrid glasses (Table 4).

The reduced porosity question of these hybrid glasses is still unresolved, but several approaches have shown exciting results in boosting porosity in these materials.[132] Some of them include the fabrication of membranes and composites comprising hybrid glasses. Alternatively, MOF-glass membranes, prepared *via* crystallite-MOF dispersion on a porous ceramic alumina support and posterior melting upon heating, have displayed excellent gas separation performances.[133] In addition, a ZIF-62 glass foam self-supported membrane has been also fabricated through the thermal decomposition of a MOF. This material has a larger number of pores and shows a great permeance of CH_4 compare to other ZIF-glasses.[134]

Another interesting approach is the incorporation of crystalline MOFs into a MOF-glass matrix to form composites.[135] Moreover, glass matrices have demonstrated the ability to retain open-pore structural phases, increasing gas uptake.[136] Recently, Knebel *et al.* have reported a synthetic approach to increase the CO_2 diffusion in ZIF-62 glass by controlling the melting and tempering parameters, resulting in changes of the pore channel structure in the ångström-range.[137] Another promising approach, still not applied in the synthesis of MOF glasses, is the use of small molecules such as carbonates, that decompose during the melting and tempering of the glass. This method has shown promise with introducing pores in inorganic glasses.[138]

As a result of the exciting properties of these glassy MOFs, this emerging field in materials science has gained great attention. These transformative materials can offer realistic solutions in luminescence, gas separation, catalysis, biomedical and optical applications with promising industrial implementation. Thanks to their intrinsic transparency and isotropic homogeneity, MOF glasses have demonstrated properties favourable to luminescence applications, especially if they contain lanthanides or luminophore ligands.[139,140] Moreover, ZIF-62 and their derivatives exhibit high transmittance ($\sim$90%)[141] and exciting nonlinear optical response for potential use in photonics.[142] Additionally, gas separation membranes containing MOF glasses have demonstrated promising results in the separation of gas mixtures, offering a

more industrial applicable approach.[133,143,144] Furthermore, imidazolate and purinate derivatives are biocompatible, which could show promise in biomedical applications such as drug delivery and scaffolds.

2.3. Solid state amorphisation

Temperature induced crystalline to amorphous transformations have been studied in detail owing to their impact on hybrid glasses in materials science. This thermal process does not involve partial or total decomposition of the linkers, and the MOF's chemical composition is retained. In 2010 the first example of an amorphous ZIF formed by thermal treatment was reported for Zn-ZIF-4 (**cag** topology) without any intermediate melting step.[120] Later, Zn-based ZIF-1, ZIF-3 and Co-ZIF-4 with topologies **crb**, **dft** and **cag**, respectively, also amorphised upon heating.[150] This effective amorphisation upon heating, without decomposition, has been linked to their topologies. Topologies such as **cag**, **BCT** or **DFT** are able to form amorphous materials without decomposition, whilst ZIF-8, ZIF-9, ZIF-11, ZIF-14, and ZIF-βqtz with **SOD**, **SOD**, **RHO**, **ANA** and **qtz** topologies respectively, decompose whilst undergoing an amorphous phase transition. Conversely, and very recently, a **SOD** topology ZIF (the same topology as ZIF-8), known as CdIF-1, has exhibited amorphisation without decomposition. After amorphisation, an improvement in diffusion and adsorption selectivities of n-C_4H_{10}/i-C_4H_{10} was observed, where it was suggested that the longer Cd–N bonds are associated with a more flexible framework, culminating in these improved properties.[151]

An exciting example of these transitions is the temperature-induced amorphisation of a Co-MOF (SCNU-Z6), [$Co_{0.7}$HL] (HL = 2,6-bis-(4-imidazol-1-yl-phenyl)-4-[4-(2*H*-tetrazol-5-yl)-phenyl]-pyridine).[152] This *a*MOF was formed by the removal of the solvent molecules in the framework over 368 K and exhibited excellent iodine capture capacity.

2.4. Amorphous to crystalline

Many studies have focused on the amorphisation of crystalline MOFs. However, despite their scarcity in the literature, amorphous-to-crystalline transformations have also been reported in MOFs. Glasses and amorphous materials are metastable, which means that they are able to transform into more stable structures and topologies with the application of high temperature over time. One of the most known MOF examples of this phenomenon is ZIF-8.

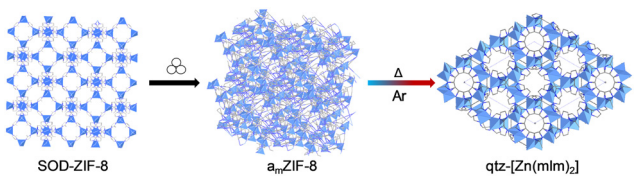

Fig. 8 Schematic depiction of the synthetic approach to obtain a new **qtz**-topology from a mechanically amorphised ZIF.[153] Reproduced from ref. 153 with permission from Royal Chemical Society, copyright 2022.

Mechanically amorphised ZIF-8 has exhibited the formation of a new, crystalline quartz topology upon heating under argon flow (Fig. 8).[153] This opens up the possibility of exploring the thermal behaviour of other a_mMOFs upon heating to obtain new desired crystalline phases.

3. Reversible high temperature phase transitions

3.1. Metal-coordination environment desolvation and guest molecules

One important characteristic of MOFs is their intrinsic porosity and their ability to host guest molecules. However, such adsorbed molecules can also be released upon heating, leading to a change in the structural conformation of the host-structure. Most guest molecules are located in the cavities of the MOF. However, there are examples where several molecules are also coordinated to the SBU, which are especially prevalent in non-porous materials and coordination polymers. It is often the case that these guest molecules interact with the host network in a supramolecular fashion.[154,155] Therefore, elimination of these coordinated and/or uncoordinated solvent molecules may result in different structural transformations with variable significance, which may be reversible or non-reversible in nature (Fig. 9).

In some cases, the exchange of coordinated solvent molecules leads to a drastic transformation across the entire framework. However, in some cases the loss of the solvent molecule results only in a slight structural distortion in the crystalline network, despite a large change in local coordination. This has been observed as colour changes in several cases. For example, a 3D magnetic MOF [$KCo_7(OH)_3(ip)_6(H_2O)_4$]·$12H_2O$ (H_2ip = isophthalic acid) underwent a reversible structural transformation to [$KCo_7(OH)_3(ip)_6$] when heated to 393 K, accompanied by a colour change from pink to purple. Upon the removal of the solvent molecules during heating, a change in the coordination geometry was observed, but without noticeable crystal lattice variations.[156] When the dehydrated purple crystals formed after the heat treatment were exposed to air for a few days, they reverted to their original red colour. Although both structures were similar, the metal coordination environments in the dehydrated compound were very different.

Some of these transitions can increase or decrease the dimensionality and the reorganising of the network. One remarkable example of this was reported by Kitagawa *et al.*[157] Here, a porous 2D coordination polymer was reversibly transformed into a 3D structure by dehydration after heating at 353 K for four hours. The material, {[Cu_2(TCI)(OH)(H_2O)$_3$]·$1.5\,H_2O$}$_n$, TCI = (tris(2-carboxyethyl)isocyanurate), contained a TCI flexible organic linker and a SBU consisting of a Cu^{II} ion. This material transforms into a 3D framework upon guest removal, caused by the sliding of the 2D sheets and contraction of the spaces between the layers. Here, versatile coordination geometry of the Cu^{II} ion and ligand flexibility played a key role in the reversible structural transformation, which was

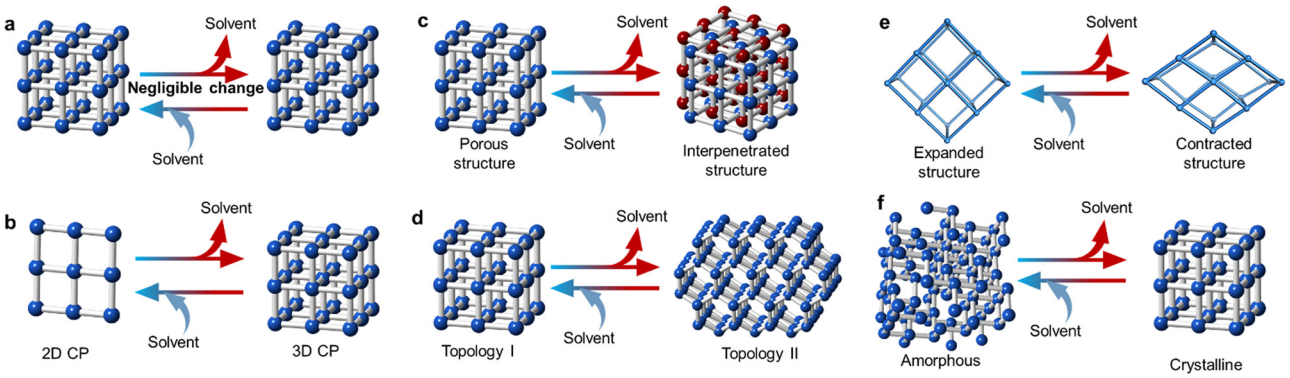

Fig. 9 Schematic depiction of the potential changes after the loss of solvent molecule. (a) Negligible changes after solvent loss. This means only changes in the coordination environment of the metal cluster occur without changes to the whole structure. (b) Increase in the dimensionality of the structure after solvent loss. (c) Creation of an interpenetrated structure. (d) Topological change after solvent loss. (e) Contraction or expansion of the structure. This behaviour is commonly known as breathing. (f) Amorphisation or recrystallisation after solvent loss. Red and blue arrows indicate heating and cooling processes, respectively.

accompanied by a change in optical and magnetic properties. Another interesting example reported by Kondo *et al.* showed a structural change from a 0D CP $\{[Co(bpy)_2(CH_3CN)_2(H_2O)]\cdot 2(OTf)\}$ (bpy = 4,4′-bipyridine, OTf = trifluoromethanesulfonate) into a 1D CP through the irreversible loss of the acetonitrile solvent after air exposure.[158] Moreover, the 1D $\{[Co(bpy)_2(OTf)_2\text{-}(H_2O)_2]\cdot(bpy)\}$ reversibility transformed into a 2D porous material, $([Co(bpy)_2(OTf)_2])$, through loss of water molecules after a thermal treatment at 423 K under vacuum. Dimensionality changes can also be reached through solvent exchange. For example, a 2D Zn-CP exhibited a transformation into a 3D-MOF after exposure to dichloromethane at room temperature, improving the framework stability, porosity and hydrogen uptake.[159]

Interpenetrated structures can also be affected by the removal of coordinated solvent molecules. One such example was MOF-123, $[Zn_7O_2(NBD)_5(DMF)_2]$ (NBD = 2-nitrobenzene-1,4-dicarboxylate), which contains DMF molecules occupying the channels.[160] By heating to 593 K, MOF-123 undergoes a structural transformation, resulting in a doubled interpenetrated $[Zn_7O_2(NBD)_5]$ material, known as MOF-246. This transformation was reversible and was associated with a 50% reduction in the thickness of the crystal after loss of the DMF molecules.

Porous structures have the capacity to accommodate a diverse range of molecules within their channels. Within the lattice, solvent molecules can engage in interactions with the host material through supramolecular bonding. Interestingly, when these solvent molecules are either lost or adsorbed, it leads to only minor alterations in the overall structure and connections within the coordination network. The chosen method for the removal of solvent molecules can cause different types of structural changes. An example of this was shown by a Mn-based MOF, $\{[Mn(L)(X)](X)_x\}_n$, where L = and X is the guest molecule = pyridine, water, dimethylformamide, 2-picoline, 4-picoline, aniline, benzonitrile or 2,6-lutidine. Depending on the guest molecule in the pore, different coordination modes of the metal centre were observed, generating materials with various space groups.[161] Another remarkable example is the dehydration of $[Cu(iba)_2]\cdot 2H_2O$ (Hiba = 4-(1*H*-imidazol-1-yl)) benzoic acid which results in different porous polymorphs depending on the dehydration method.[162] When the crystal was heated at 433 K for 12 hours, the product CP retained the original topology. However, when exposed to air at room temperature for two months, a 2D complex, $[Cu(iba)_2]$, was formed instead. Kinetic and/or thermodynamic processes are thought to control the different routes.

In most flexible porous materials, the reversible loss of the solvent serves as a distinctive feature, inducing a disruption within the host structure without the breakage or formation of new chemical bonds. This unique characteristic highlights the adaptability of these materials to environmental changes. Despite the absence of bond rearrangements, the intricate interplay of multi-variable coordination geometries exhibited by metal ions, the dynamic nature of metal–ligand bonds, and the arrangement of supramolecular packing contribute significantly to structural transformations. As an example, tetragonal $[Ag_6Cl(atz)_4]OH\cdot 6H_2O$ (Hatz = 3-amino-1,2,4,-triazole) can be dehydrated reversibly to obtain $[Ag_6Cl(atz)_4]OH\cdot xH_2O$.[163] Here, the host framework structure has a large distortion from the original one, but the topology of the $[Ag_3(atz)_2]$ network is retained with similar structural parameters. Both structures exhibited a six-fold interpenetration. Another example showed a dynamic MOF, CCIQS-1, exhibit different phase transitions as a result of solvation and desolvation processes.[164] Desolvation of the as-synthesised phase shows a phase transition from $Cmc2_1$ to $P2_12_12_1$, accompanied by a contraction of the unit cell and the opening of the hydrophilic channels. This process was selectively reversible by soaking the material in different solvents, such as DMF, THF, 1-hexene or mixtures of DMF and toluene.

Another interesting behaviour observed in the loss of solvent molecules is the structural memory effect. For example, Du *et al.* reported a reversible crystal-to-amorphous phase

transition of a sponge-like MOF, $[Mn(Me\text{-}ip)(DMF)]_n$, (Me-ip$H_2$ = 5-methylisophthalic acid) to an amorphous phase, in which DMF molecules were released upon heating above 453 K. The crystallinity of this phase was recovered after 48-hour immersion in DMF.[165] This material exhibits a crystalline-amorphous-crystalline behaviour recovering its crystalline structure from an amorphised structure. This memory effect can also be delayed, which decreases the crystallite-size whilst maintaining a mesostable open-pore phase when the solvent is removed. The close-pore phase is recovered after a thermal treatment. A remarkable example is $[Cu_2(bdc)_2(bpy)]_n$, a porous framework reported by Kitagawa *et al.* where 50 nm crystallites in their dried form maintained the open-pore phase.[166] However, >100 nm particles contained a mixture of phases (closed and open-pore phase) and crystallites with sizes over 300 nm exhibited a pristine closed-pore phase.

Guest loss in MOFs upon heating can also be used in sensing. For example, multiple MOFs have been investigated as volatile organic compounds (VOCs) colorimetric sensors thanks to their colour change after the VOC is removed.[167,168]

An interesting example is a luminescent cationic MOF, $[\{Zn(L)(MeOH)_2\}(NO_3)_2{\cdot}xG]_n$ (where L is 4,4′-ethylenedianiline and 2-pyridine-carboxaldehyde, and G are disordered guest molecules).[169] The structure of this MOF changed drastically, in a reversible way, with the loss of methanol or water molecules, which led to changes in the shapes and sizes of the pores. In addition, the anion in this MOF can be easily exchanged with anions (ClO_4^-, SCN^-, N_3^- and $N(CN)_2^-$), which enabled tuning of their luminescent properties, accompanied by expansion or contraction of the unit cell. A similar behaviour was observed in a layered Zn-MOF with nitrate anions located in the interlayer channels. In this example, anions could be exchanged, generating three different topologies depending on the nature of the guest anion.[170]

3.2. Gate opening and closing in flexible MOFs.

Typically, upon heating, materials expand in three dimensions because of the increased vibrations of their constituent atoms.[171] In addition to positive expansion, unusual structural arrangements can lead to unexpected thermal expansion behaviours, such as negative (contraction) or zero. Several MOFs show a reversible change in their unit cell parameters, whilst maintaining their composition after thermal treatment. They are known as thermoresponsive MOFs.[10] Thanks to their flexibility, MOFs often exhibit these anomalous behaviours.[172] For example, MOF-5,[173] IR-MOFs[174] and HKUST-1,[175] have shown remarkable experimental and theoretical negative thermal expansion (NTE). Moreover, MOF-339 has the largest theoretical negative thermal expansion value reported to date.[176] However, this material is not accessible experimentally because of its low mechanical stability. Another example of anomalous behaviour is the anisotropic thermal expansion demonstrated by HMOF-1.[177] In this example, the *a* cell parameter increased, *b* decreased and the *c* parameter remained unchanged upon heating. Additionally, a Zn-based MOF, $[[Zn(napht)_2(OH)_2]_n{\cdot}n CH_3OH]$, exhibited a large anisotropic thermal expansion of its network at 370 K.[178] More specifically, this anisotropic behaviour involved positive thermal expansion (PTE) along the *c* axis accompanied by biaxial NTE along the *a* and *b* axes. A remarkable example reported by Kaskel *et al.* is (Cu)DUT-69, $[Cu_2(BBCDC)]X_n$ (X = solvent), which showed a change in the material's thermal behaviour from positive to negative thermal expansion, depending on the presence of solvent guest molecules.[179] This behaviour could be tuned depending on the transition metal selected.

Flexible MOF systems can be categorised according to the type of metal-node and how their coordination chemistry with the linker molecules controls the framework dynamics.

One type of distortion that has been observed in flexible MOFs has been termed breathing behaviour. This phenomenon is associated with reversible structural transitions of MOFs, where atoms are substantially displaced in the framework and the unit cell volume changes.[10] These materials are able to transform between closed or narrow pore (**np**) to open or large pore (**lp**) conformations (Fig. 10). Unit cell parameters and crystallographic space groups of the distinct phases (narrow pore and large pore) are frequently different. Pioneering groups in this field include those of G. Ferey and S. Kitagawa, who have expanded this concept since 2004.[180]

Similarly, various research groups have developed new, highly breathable frameworks. These frameworks can be adjusted in terms of their flexibility, rigidity, and how much

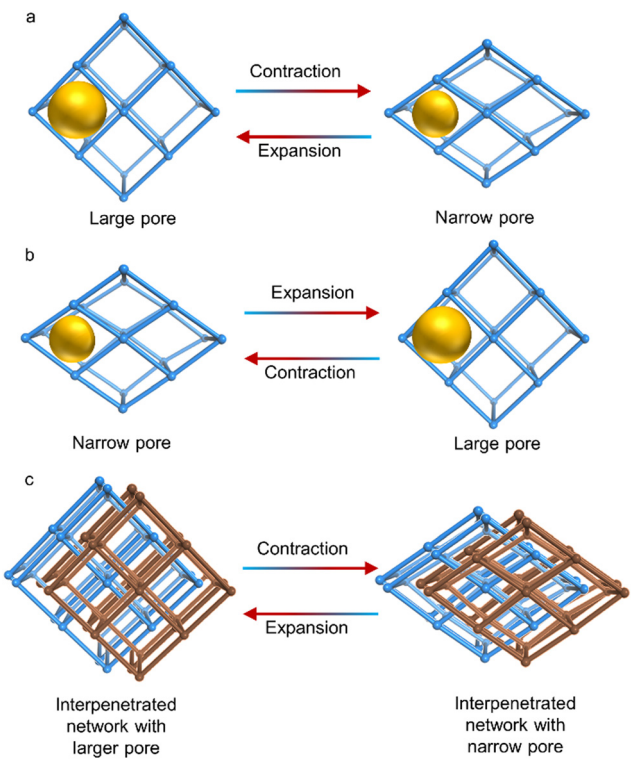

Fig. 10 Schematic depiction of gate opening and closing processes. (a). Contraction of the unit cell upon heating. (b) Expansion of the cell upon heating. (c). Contraction of the cell upon heating with an interpenetrated structure. Yellow spheres indicate the pore size and red and blue arrows show heating and cooling processes, respectively.

they can expand and contract by using specific solvent molecules within their lattice structures.[156,181] One framework, namely $[Zn_3(OH)_2(btca)_2]\cdot DMF\cdot 4H_2O$ (H_2btca = benzotriazole-5-carboxylic acid),[182] exists in a large pore phase, which then transforms into a small pore phase, $[Zn_3(OH)_2(btca)_2]$, at 713 K for 30 minutes. Two intermediates were identified at 493 K, $[Zn_3(OH)_2(btca)_2]\cdot DMF\cdot 0.5H_2O$ and $[Zn_3(OH)_2(btca)_2]\cdot 2H_2O$. Another example is $Co(BDP)\cdot 2DEF\cdot H_2O$, with DEF molecules present in the channels.[183] Upon heating to 443 K, desolvation of these molecules occurred, generating a substantially different structure. The original structure was regenerated by exposing the desolvated one to DEF. These findings align with a flexing behaviour similar to an accordion, which alternately narrows and widens the channel pores. This behaviour has been previously shown in similar frameworks linked by terephthalate.[184]

One of the most remarkable examples of breathing was reported by C. Serre *et al.* in 2008.[185] They observed that expansion upon solvent adsorption occurs without apparent bond breaking, in a series of isoreticular chromium and iron dicarboxilates with formula $[M_3^{III}O(H_2O)_2X(fum)_3]\cdot$guest (M = Fe, Cr; X = F, Cl, acetate), labelled MIL-88A to D [fum = fumarate (88A), terephthalate (1,4-BDC) (88B), 2,6-naphthalenedicarboxylate (NDC) (88C), and 4-4′-biphenyldicarboxylate (BPDC) (88D)]. The as-synthesised forms were able to accept solvents to produce the open form. However, heating and desolvating directly produced the dry form.

Apart from the expansion and contraction behaviour and the deformation of the coordination framework, sliding between closely packed layers or networks caused by guest exchange, dehydration, and sorption can also change the structure of a porous material.[186] In certain cases, this process leads to a change in the packing mode. One of the first examples of this behaviour was a laminated framework, $[Fe(pydc)(4,4'\text{-bipy})]\cdot H_2O$ (H_2pydc = 2,5-dicarboxypyridine, 4,4′-bipy = 4,4′-bipyridine).[187] Here, authors observed structural contraction and reversible sliding of the layers in the material even though the space group and lattice parameters were maintained after heating. An interesting example of expansion in the unit cell and channel size was observed in the partially interpenetrated NOTT-202 material $([Me_2NH_2]_{1.75}[In(C_{40}H_{22}O_8)]_{1.75}\cdot 12(C_3H_7NO)\cdot 10H_2O)$.[188] Guest removal of the material led to a structural phase transition with a change of symmetry from orthorhombic to monoclinic and a cell volume expansion of 11%.

Structural variation caused by the presence/absence of solvent molecules is not the only change that can occur with MOFs, changes in physicochemical properties such as colour can also take place. An illustrative example is the robust MOF $[Ni(cyclam)(bpydc)]\cdot 5H_2O$ (cyclam = 1,4,8,11-tetraazacyclotetradecane, $bpydc_2^-$ = 2,2′-bipyridil-5,5′-dicarboxylate), which underwent dehydration concomitant with a colour change from yellow to pink when heated to 423 K.[189] When the dehydrated crystal, [Ni(cyclam)(bpydc)], was subjected to air or water vapour for several minutes, the crystal returned to its original yellow colour. Notably, both processes occured while maintaining crystallinity, indicating preservation of the crystal structure with only a minor variation in the unit cell parameters. This suggests that exposure to air or water vapour leads to reversible changes in the crystal.

A new phenomenon that has emerged in MOF-composites is the ability to lock the wide-pore or large-pore phase of the MOF, even after complete desolvation. ZIF-7, $[Zn(bIm)_2]$ (bIm = benzimidazolate), exhibits a phase transition between wide-pore (ZIF-7-I) and narrow-pore (ZIF-7-II) as a result of desolvation. ZIF-7-I was locked by a mixed-matrix membrane containing ZIF-7-I nanocrystals and rigid polyimides. Retaining this wide-pore structure increased the selectivity and permeability for O_2/N_2 separation.[190]

Crystal engineering can also be used to control breathing processes. A recent study showed that an isostructural MIL-53 MOF, NU-2002 with formula $[Al(OH)(BPDCA)]_n$ (BPDCA = bicyclo[1.1.1]pentane-1,3-dicarboxylic acid), displayed increased efficiency in separating hexane isomers. This was achieved by increasing the linker dimensionality by using a 3D linker, BPDCA, instead of a 2D linker, terephthalic acid. This in turn controlled the structural breathing of the MOF.[191]

3.3. Conformational changes

The alterations in MOF structure triggered by temperature fluctuations can result in either polymerisation or depolymerisation processes, involving the breaking or formation of bonds and prompting movements within the lattice. Additionally, this rearrangement has the potential to influence the dimensionality of the material, meaning it can impact the spatial arrangement or configuration of the compound in terms of its three-dimensional structure. One example reported by Zhou *et al.* showed how a hydrated phase, $[Cu(tzc)(dpp)]_n\cdot 2H_2O$, transformed into an anhydrous phase $[Cu(tzc)(dpp)]_n$ *via* the monohydrate intermediate phase $[Cu(tzc)(dpp)]_n\cdot H_2O$.[192] Upon heating to 423 K, the $[Cu(tzc)(dpp)]_n$ phase transformed into a new orthorhombic polymorph which was then transformed into a monoclinic phase upon cooling at 100 K (Fig. 11). These polymorphs exhibited different magnetic behaviour.

Thallapally *et al.* showed that a heterometallic MOF, $\{[Yb_6Cu_{12}(OH)_4(PyC)_{12}(H_2O)_{36}]\cdot(NO_3)_{14}\cdot xS\}_n$ (where H_2PyC = 4-Pyrazolecarboxylic acid, S = unassigned free solvent molecules), transformed into a different phase, $\{[Yb_4O(H_2O)_4Cu_8(OH)_{8/3}(PyC)_8(HCOO)_4]\cdot(NO_3)_{10/3}\cdot xS\}_n$, upon heating above 393 K.[193] The channel sizes and topologies of the two phases were identical, but structural changes were observed in the metal nodes by single-crystal X-ray diffraction (SCXRD). These changes were also probed by *ab initio* molecular dynamics simulations.

4. Low temperature phase transitions

Examples of phase transitions in MOFs occurring at room temperature or below are less common than those at high temperatures. A possible explanation for this is that thermal stability is usually studied at higher temperatures to identify the decomposition temperature of the material and to monitor

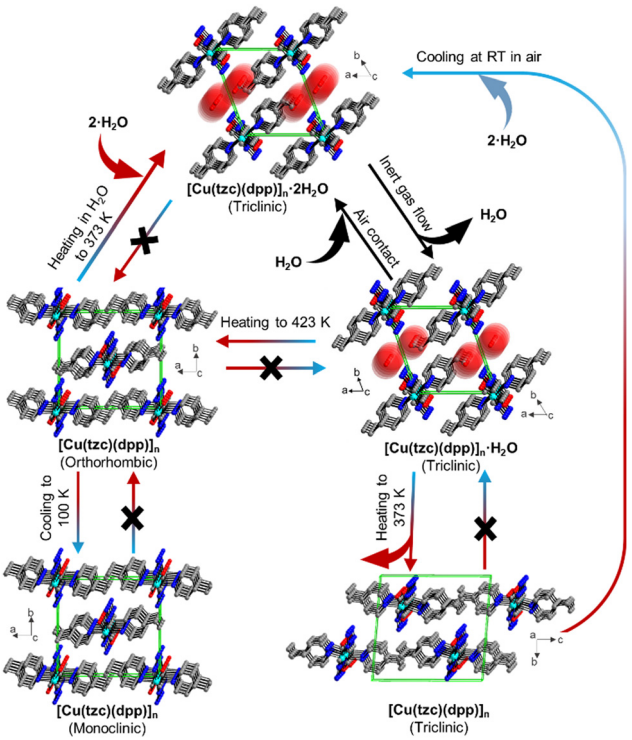

Fig. 11 Crystal structures of the hydrates $[Cu(tzc)(dpp)]_n{\cdot}2H_2O$, $[Cu(tzc)(dpp)]_n{\cdot}H_2O$ and their polymorphic anhydrate modifications $[Cu(tzc)(dpp)]_n$ viewed as stacked chains in a single unit cell. Arrows and labels indicate the directions and conditions, respectively, for phase transitions occurring between these phases.[192] (tzc: tetrazolate-5-carboxylate, dpp: 1,3-di(4-pyridyl)propane).

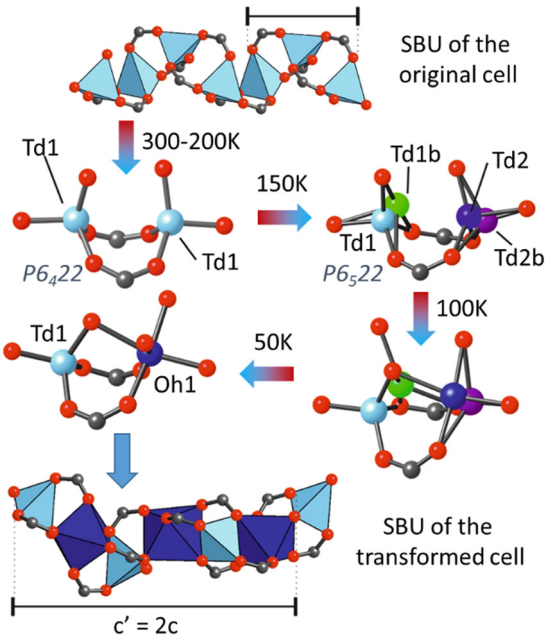

Fig. 12 Schematic depiction of the structural transition occurring in the $[Zn_{0.79}Co_{0.21}(hfipbb)]$ material upon cooling. The inorganic SBU might adapt to include octahedrally coordinated cations, which results in a unit cell transformation with a doubled *c* parameter.[195] Image modified with permission of Science.

the potential loss of solvent molecules. As such, many potential structural phase transitions occurring at lower temperatures may be present, yet unobserved. This is surprising considering that one of the most promising applications of MOFs is gas capture and separation, where isotherms of N_2, H_2, CO_2, and others, are collected below room temperature, where structural transitions could affect the MOF's capture and separation ability.

In most cases, structural phase transitions caused by cooling below room temperature are reversible. An interesting example is the structural study of PCN-526, $[Cd_8C_{96}H_{48}Cl_5N_{40}O_6]$.[194] Here, the phase transition occurred at 110 K. The authors demonstrated that during this phase transition, the one-dimensional channel of the MOF was distorted from a square to rectangular shape, whilst maintaining its crystallinity. Additionally, the mechanism for the transformation was linked to the modification of the occupancy or species of metal ions in the cavities.

Another illustrative example is a MOF with a rod-shaped SBU, $[Zn_{0.59}Co_{0.41}(hfipbb)]$ [(hfipbb = 4,4′-(hexafluoroisopropylidene)-bis(benzoic acid))], which exhibited a doubling of cell volume at low temperature.[195] According to variable temperature single crystal X-ray diffraction experiments, the lattice parameter *c* doubled when cooling to 150 K from room temperature as a result of a phase transition. At room temperature, data showed the presence of only one tetrahedral metal site, with a mixed Zn/Co occupancy. A phase transition was first observed at 150 K, with the corresponding doubling of the *c* parameter. After the phase transition, two independent crystallographic metal positions appeared in the SBU, exhibiting a tetrahedral-distorted coordination, denoted as Td1 and Td2 in Fig. 12. Analysis of the difference Fourier maps revealed a large residual electron density around the metal positions, which were assigned as additional metal sites with partial occupancy (Td1b and Td2b), arising from the ongoing atomic rearrangement. However, the presence of residual electron density indicated that the transformation was not complete until 50 K. At this temperature, the crystal structure was equivalent to one with the composition $Zn_{0.21}Co_{0.79}$(hfipbb), with both octahedral and tetrahedral metal sites. These results suggested that an increment in the cobalt content in the SBU had a stabilising effect on the octahedral site.

Another example, $[Ag_6Cl(atz)_4]OH{\cdot}6H_2O$ (Hatz = 3-amino-1,2,4,-triazole) with a tetragonal phase can be transformed into an orthorhombic phase at 103 K.[163] The amino groups in both cases were two-fold disordered. When the orthorhombic phase was heated to 293 K, it slowly transformed back to tetragonal.

A similar, reversible structural transformation occurs in DUT-7, $Zn_4O((S)\text{-}L)_3(DMF)_{10}(H_2O)_{3.5}$ ((S)-L = 2,2′-spirobiindane-5,5′-dicarboxylic acid), upon cooling to 100 K.[196] During this transformation, a notable change occured where one of the zinc atoms within the Zn_4O cluster transitioned from a tetrahedral to an octahedral environment. This shift was caused by the coordination of two additional solvent molecules. This demonstrates cluster flexibility, a phenomenon that can provide fresh perspectives on the catalytic activity of MOFs.

5. Characterisation of phase transitions

5.1. Thermal characterisation

Thermogravimetric analysis (TGA) is a widely applied characterisation technique used for the thermal analysis of MOFs because of its availability and straightforward analysis.[11] It records mass loss of the sample upon heating at a specific heating rate under a specific atmosphere. TGA data usually provide useful information to calculate the composition, defect concentration and the solvent molecules present in a MOF's pores.[197] It also provides the decomposition temperature (T_d) of MOFs and can be used to calculate the composition of a material after heating. This is particularly useful for the preparation of MOF-derived materials described in the non-reversible phase transitions section.

However, TGA has some limitations, such as low resolution for the majority of the available data because of the large temperature intervals (50 or 100 K). In addition, clearly identifying the difference between the plateau of the TGA curve and the decomposition curve is sometimes challenging, especially when solvent loss is involved. This makes it difficult to identify the different decomposition steps. The TGA curve is also sensitive to experimental factors such as heating rate, heating atmosphere and the pre-treatments carried out. This causes substantial differences in T_d values for the same material,[198] which means that experimental details should be reported alongside T_d. The idea of thermal stability in general is somewhat misrepresented, where it can be argued that classifying a material as thermally stable at a given temperature requires isothermal experiments to recreate actual working conditions.

As such, TGA data are not enough to fully characterise the thermal properties of MOFs; TGA analysis should be accompanied with differential scanning calorimetry (DSC) and a crystallographic characterisation technique, such as X-ray or neutron diffraction.

Differential scanning calorimetry has become, in addition to TGA, a universal standard tool for the characterisation of phase transitions, owing to its ultrahigh sensitivity to small energy fluctuations. A typical DSC experiment consists of heating a sample dynamically or isothermally by applying heat flow under a specific atmosphere. Both the sample and a reference are monitored as a function of time and temperature.[199] The calorimeter measures the heat/energy absorbed (endothermic reaction) or released (exothermic reaction) by the sample when it is subjected to a specific temperature path (Fig. 13).[200]

This information is also particularly important for differentiating between glassy and amorphous MOFs, where glassy MOFs have a T_g, and amorphous MOFs do not. It is also useful for identifying melting processes and the melting temperature of a material.

5.2. X-ray and neutron diffraction

Several spectroscopic techniques have been developed to provide structural information of materials, crystallography is still the most important and straightforward method to visualise 3D MOF structures and their structural changes.

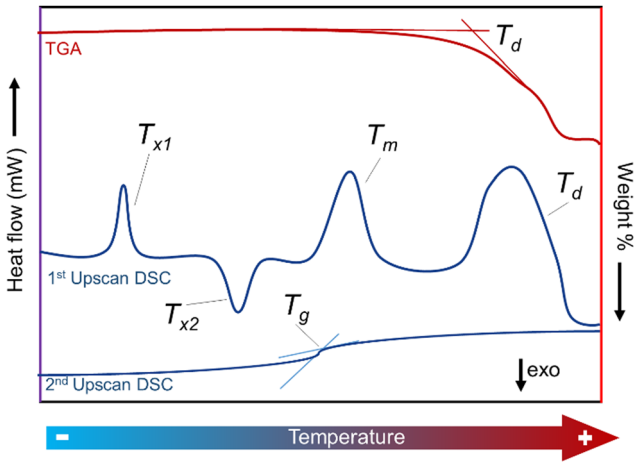

Fig. 13 DSC depiction (Heat flow *vs.* Temperature) and thermogravimetric analysis of a meltable crystalline MOF. TGA is represented as a red line showing a weight loss upon heating, indicating the decomposition temperature (T_d). DSC 1st and 2nd upscans are depicted in the graph as blue curves. 1st upscan shows multiple processes upon heating. Firstly, an endothermic recrystallisation (structural phase transition) denoted as T_{x1}. The second feature shows an exothermic phase transition (T_{x2}). Melting and decomposition processes also appear as endothermic features. A T_g appears in the 2nd DSC upscan of a crystalline MOF, after the material melted and formed a glassy phase during heating in the 1st upscan.

Microcrystalline powders are generally more readily available than single crystals. However, due to extensive overlap of diffraction peaks, powder X-ray diffraction (PXRD) patterns offer comparatively less structural information with less accuracy compared to SCXRD experiments. Additionally, *ab initio* determination of unknown and complex crystal structures from PXRD data remains a substantial, and sometimes impossible, challenge. In contrast, solving structures from SCXRD data has become a routine and reliable method.[201] SCXRD patterns measured using common in-house X-ray sources can provide precise atomic coordinates, bond lengths, bond angles, as well as information on atomic thermal displacements and occupancies. Such detailed structural insights are generally unavailable from PXRD, even when measured using highly monochromatised and intense synchrotron radiation. The inherent limitations of PXRD underscore the continued importance and utility of SCXRD for obtaining accurate and comprehensive crystallographic data.

However, it is not always possible to obtain single crystals with MOF materials. Although PXRD is more challenging for structure solution, it is possible to solve structures using multiple crystallographic approaches such as direct methods[202] or charge-flipping methods.[203]

In addition, neutron diffraction experiments can also be employed to monitor structural phase transitions and processes, despite the lack of examples in MOFs. Although most organic linkers contain hydrogen atoms, which contribute to the diffraction pattern by increasing the background, this technique may be useful to study the contribution of multiple

phases at variable temperatures (VT). An example is the VT study of a bimetallic MOF, $[Zn_{1-x}Co_x(hfipbb)]$ containing two different metals. The presence of two different phases with different metal sequences in their SBUs were observed through Rietveld refinement of the VT-neutron diffraction data.[195]

5.2.1. *In situ* studies. Reviewing the recent progress in the use of *in situ* characterisation techniques, as well as theoretical approaches to better understand the mechanism of phases transitions and breathing, is crucial for several applications. However, these types of studies are still scarce.

One of the most remarkable studies shows the polymorphism of ZIF-4 through the collection of multiple measurements at variable pressure and temperature. With this information, a pressure–temperature phase diagram was prepared (Fig. 14).[204] These types of experiments can be extended to different MOFs to construct similar phase diagrams, and to explore unknown structures in *operando* mode, which will have a great impact on their industrial implementation.

5.3. Characterisation techniques of local structure

Total X-ray and neutron scattering experiments to extract the pair distribution function (PDF) have gained attention in recent years to analyse defective and highly disordered MOF materials. This technique analyses both Bragg and diffuse scattering signals simultaneously and is thus ideal to analyse MOFs.

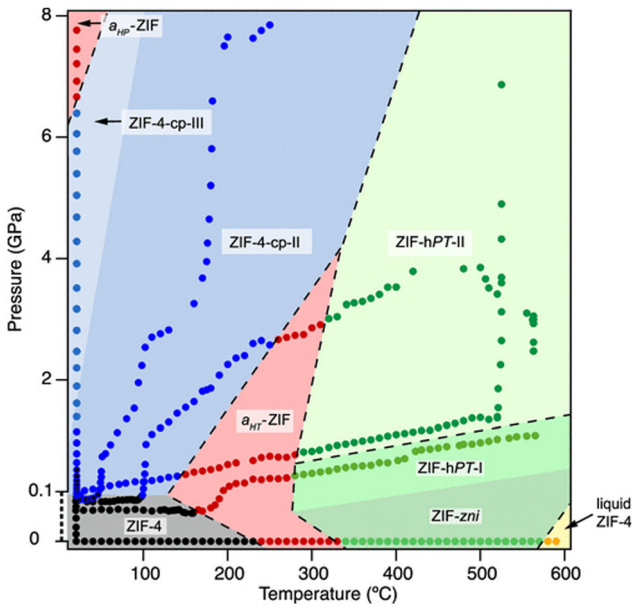

Fig. 14 Pressure–temperature phase diagram of ZIF-4. The pressure range from 0 to 0.1 GPa has been magnified for better visibility and is thus not to scale. Experimental points are represented as circle symbols, and they are coloured according to the phases observed *in situ* (ZIF-4 cag: black, ZIF-4cp-II: blue, amorphous ZIF: red, ZIF-zni: green, ZIF-liquid: yellow). Coloured outlines of phase boundaries are drawn as guides to the eye. Dashed lines indicate irreversible, reconstructive transition.[204] Reproduced from ref. 204 with permission from American Chemical Society, copyright 2019.

PDF gives information in real space instead of reciprocal space, as diffraction. This gives key information on the local structure of both crystalline and amorphous MOFs.[205]

This technique is particularly important for the characterisation of MOF glasses, which lack long-range order, and it allows comparison of the local structure of a crystalline MOF with its glassy analogue. Moreover, multivariate and linear regression analysis of PDF data provides information about the atom–atom interactions at the interface of MOF-composites.[206,207] In addition, *in situ* PDF experiments are an effective way to monitor melting and vitrification processes, providing insights into changes in the local structure upon heating.

These *in situ* experiments also unveil local distortions. One interesting example was reported by Platero-Prats *et al.*, in which NU-100 and UiO-66 were studied by VT-PDF measurements.[208] Structural transitions of the Zr_6- and Hf_6-nodes in both structures, only visible when observing their local structures by VT-PDF, were deciphered (Fig. 15). These phase transition are important to understand as they may affect the catalytic activity of these materials.

The structural dynamics of the local structure of MOFs can also be monitored by spectroscopic techniques, such as X-ray absorption spectroscopy (XAS). One example of utilising this technique was a study on a Ca-MOF, Ca(BDC)(DMF)(H_2O), which has the same topology of MIL-53. Loss of the DMF molecules on the surface of the MOF crystallites occurred before the decoordination of the solvent. This study suggested that the DMF was already partially decoordinated at 423 K in different domains, in agreement with NMR analyses. The phase transition was completed at 673 K, also confirmed by XRD Rietveld refinement.[209]

5.4. Microscopic techniques

Transmission electron microscopy (TEM) has been employed by MOF researchers to study dynamic processes of MOFs because of recent developments in camera and detector technology, which allows diffraction studies to be performed using a very small amount of sample, with minimal beam damage.[210]

Development of microscopic techniques has allowed researchers to study dynamic processes in different soft materials, such as phase transitions and self-assemblies.[211,212] However, examples of MOF studies are still rare because of the

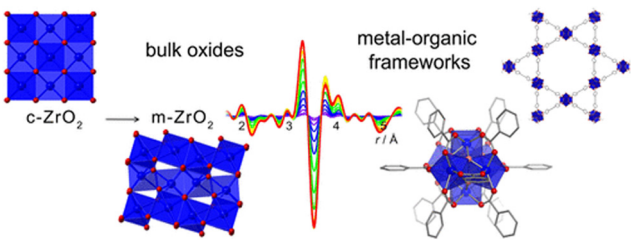

Fig. 15 Schematic depiction of the metal-node phase transition of NU-1000 and UiO-66 structures upon heating.[208] Reproduced from ref. 208 with permission from American Chemical Society, copyright 2017.

experimental limitations observing the spatiotemporal evolution of their structures.

Microscopic *in situ* experiments using variable temperature liquid-cell transmission electron microscopy (VT-LCTEM) aim to solve this issue. This promising approach has been used to study the growth mechanisms of ZIF-8.[213] In another example, VT-LCTEM, combined with HRTEM, enabled the observation of a phase transition from a microporous MOF, **scu**-NU-906, to a mesoporous MOF, **csq**-NU-1008, $[Zr_6O_4(OH)_8(OH_2)_4(TCPB\text{-}Br_2)_2]$ ($TCPB\text{-}Br_2$ = 1,4-dibromo-2,3,5,6-tetrakis(4-carboxyphenyl)benzene) (Fig. 16).[214] Moreover, *in situ* TEM has been recently used to construct phase diagrams of many Zr-MOFs, providing information on phase, crystallinity, crystallite size and morphology.[215]

Another *in situ* approach is ultrafast transmission electron microscopy (UTEM), using dark-field imaging. This promising methodology has been employed to solve tantalum disulphide charge-ordered phases.[216]

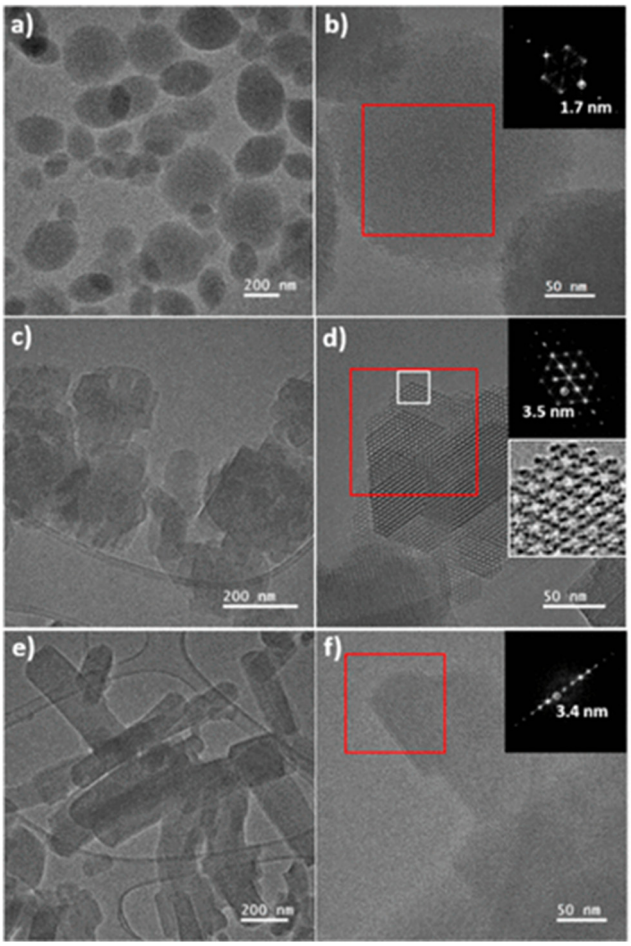

Fig. 16 TEM images during the reaction of the phase transition transformation over time by the addition of formic acid to NU-906. (a) and (b) NU-906, (c) and (d) NU-1008 isolated after two hours (e) and (f) NU-1008 isolated after two days. Insets: Fast Fourier transform (FFT) of the image inside the red square, cropped at the predominant lattice fringes, and enlarged image inside the white square.[214] Adapted from ref. 214 with permission from the American Chemical Society, copyright 2020.

Temperature control when using microscopes is still a challenge, but these microscopic approaches will be able to monitor thermoactivated phase transitions in an image, and also in a diffraction mode, in the near future.

6. Theoretical calculations and modelling

Theoretical calculations and modelling methods have been extensively used in recent years to complement experimental work and to help researchers better understand material structures and properties.

Density-functional theory (DFT) is probably the most extended computational quantum mechanical modelling approach used in materials science to investigate structural configurations of materials. DFT methods have been used in MOF chemistry to calculate diffusion activation energies,[217] elucidate gas adsorption sites[218] and to understand mechanical[219] and luminescent properties.[220]

Structural determination of amorphous structures at the microscopic or bulk scale is always challenging. Despite the tremendous efforts using total scattering and different microscopic, diffractometric and spectroscopic techniques, often only information at the local scale is obtained.

To address this challenge, multiple computational methods have been applied to model these highly disordered structures. Several strategies have been employed to generate potential models. For example, several strategies involve simulating a phase transition from the parent crystalline MOF to an amorphous one using molecular dynamics (MD). Some *ab initio* MDs have been successfully used to simulate the melting of crystalline MOFs to their liquid state,[221,222] and to model the corresponding melt-quenched glasses.[223] However, the formation of most amorphous MOFs requires the simulation of bond breaking and reformation, which considerably increases the computational cost of this method.[224] Therefore, reactive force fields (ReaxFF) have been also proposed as an alternative approach, a compromise between chemical accuracy and computational cost. This method, which has connection-dependent terms, enables the simulation of breaking-reformation processes in atomic bonds.[225]

However, glass-MOF models obtained through ReaxFF have been found to be remarkably different from the *ab initio* counterparts, in both local and medium scale, as well as in the bulk properties.[226]

A rare example of a mixed-linker metal–organic framework incorporating a semi-rigid ditopic diacetylene ligand is UMON-44, $\{[Zn(L_1)(L_2)](DMF)_2\}_n$ (L_1: 1,6-bis(1-imidazolyl)-2,4-hexadiyne, L_2: isophthalate).[227] This flexible structure revealed two phase transitions upon heating, and the presence of large positive and negative thermal expansions. Computational methods effectively differentiated between two polymorphs of UMON-44 by precisely replicating their essential structural and spectroscopic features. This was done by extrapolating free energies at finite temperatures

and checking the specific temperature a phase became more stable than the preceding one.

Breathing behaviour mechanisms have also been studied by MD within artificial periodic boundary conditions to simulate crystalline materials using small unit cells and non-defective MOFs.[228] For example, the method of breathing of the MIL-53 material has been exhaustively analysed in the last years. Original studies of the breathing mechanism suggested that the phase transition occured in a cooperative manner through Monte Carlo simulations, where the transformation was layer-by layer.[229] However, more recent studies strongly contest this. Body dispersion calculations within a random-phase approximation suggest that even at 0 K, a small fraction of the large-pore phase is still present.[230]

More realistic force-field-based MD have been recently used, which enable large-scale cells. These results suggest this phenomenon has its origin in spatial disorder as interfacial defects, as a consequence of thermal treatments, generating unknown phases coexisting with the known crystalline ones.[228] This was also confirmed using non-periodic nanocrystallite models in other MOFs, such as DMOF-1 and DUT-128.[231]

7. Conclusions and perspectives

Multiple thermally activated processes, which may be reversible or irreversible, can occur upon heating a MOF.

Typically, non-reversible processes are related to the total or partial decomposition of the linker. The control of the thermal and atmospheric parameters during heating are crucial to obtain the desired MOF-derived nanostructures. These derived materials are widely employed for electrochemical and catalytic applications.

Other non-reversible processes such as structural phase transformations have been classified and described in detail. Several MOFs and 3D CPs can melt and form a liquid state, with the ability to form melt-quenched glasses after rapid cooling. Despite the scarcity of melt-quenched MOF glasses, this new branch of the MOF field has received great attention thanks to the promising mechanical and optical properties of MOF glasses. Less common transitions upon heating, such as crystalline to amorphous (non-glassy) and amorphous (non-glassy) to crystalline are also possible.

Reversible structural phase transitions are mostly related to the loss of solvent molecules. For example, the phenomenon of breathing has received great interest in the MOF-field because of the different porosities (and thus guest sorption behaviours) that can be reached upon heating.

Other conformational changes can also appear upon heating in a reversible way, with or without decoordination of a solvent molecule.

Low temperature structural phase transitions were also reviewed here. Even though reports are still rare at present, they may have a fundamental impact in gas sorption and magnetic studies.

Characterisation of phase transitions are crucial to understand their nature and also to identify the initial and the transformed structure. In this regard, *in situ* experiments will become crucial to monitor phase transitions.

Multiple techniques must be employed to identify different phase transitions. Thermal analysis through TGA and DSC allows differentiation between amorphous and glass phases. Additionally, diffractometric techniques give structural information through single crystal or powder analysis.

Advances in electron microscopy will also allow further in-depth monitoring of phase transitions in MOFs. This developing field will have a tremendous impact on the identification and monitoring of phase transitions in diffraction and image mode.

These advances in characterisation and increased focus on the understanding of diverse structural transitions in MOFs will have significant effects tremendous impact on the MOF field because of the link between structural variation and transitions and the MOFs physical and chemical properties.

Abbreviations

3-Pybpy	[3,1′:4′,4″terpyridin]-1′-ium
5-Cl-2-mbIm	5-Chloro-2-methylbenzimidazolate
5-FbIm	5-Fluorobenzimidazolate
5-ClbIm	5-Chlorobenzimidazolate
6-Cl-5-FbIm	6-Chloro-5-fluorobenzimidazolate
BBCDC	Biphenyl bis(carbazole dicarboxylate)
bIm	Benzenimidazolate
bpee	*trans*-1,2-bis(4-pyridyl)ethylene
bpy	4,4′-Bipyridine
C2bpy	1-Ethyl-[4,4′-bipyridin]-1-ium
C4bpy	1-Butyl-[4,4′-bipyridin]-1-ium
dCNIm	4,5-Dicyanoimidazolate
DEF	Diethylformamide
DFT	Density functional theory
DMF	Dimethylformamide
DSC	Differential scanning calorimetry
FFT	Fast Fourier transform
fum	fumarate
H_2hfipbb	4,4′-(Hexafluoroisopropylidene)bis(benzoic acid)
H_2BDC	Benzenedycarboxylic acid
HL	2,6-Bis-(4-imidazol-1-yl-phenyl)-4-[4-(2*H*-tetrazol-5-yl)-phenyl]-pyridine
H_2PyC	4-Pyrazolecarboxylic acid
H_2TTPP	5,10,15,20-Tetrakis[4-(2*H*-tetrazol-5-yl)phenyl]porphyrin
H_3BTC	Benzenetricarboxylic acid
Hatz	3-Amino-1,2,4,-triazole
HMOF	Hinged metal–organic framework
HPC	Hollow porous carbon
Im	Imidazolate
L1	Isonicotinate
L2	Pyridine-3-carboxylate
L2Br	3-Bromoisonicotinate
L2Cl	3-Chloroisonicotinate

L2F	3-Fluoroisonicotinate
$L2NH_2$	3-Aminoisonicotinate
L3	(*E*)-3-(Pyridin-4-yl)acrylate
L4	4-(Pyridin-4-yl)benzoate
L5	(*E*)-4-(2-(Pyridin-4-yl)vinyl)benzoate
L6	4-(1*H*-imidazol-1-yl)benzoate
mIm	2-Methylimidazolate
mL1	1,3,5-Tris((3-cyanophenylethynyl)benzene)
MD	Molecular dynamics
MOF	Metal–organic framework
MUV	Materials of the University of Valencia
napht	4-(1*H*-naphtho[2,3-*d*]imidazol-1-yl)benzoic acid
NBD	2-Nitrobenzene-1,4-dicarboxylate
pL2	1,3,5-Tris(4-ethynylbenzonitrile)benzene
Phbpy	1-Phenyl-[4,4′-bipyridin]-1-ium
Pur	Purinate
PDF	Pair distribution function
PXRD	Powder X-ray diffraction
SEM	Scanning electron microscopy
ted	Triethylenediamine
TEM	Transmission electron microscopy
TGA	Thermal gravimetric analysis
$TCPB\text{-}Br_2$	1,4-Dibromo-2,3,5,6-tetrakis(4-carboxyphenyl)benzene
UTEM	Ultrafast transmission electron microscopy
ZIF	Zeolitic imidazolate framework

Author contributions

C. C. B. conceptualised this review. All authors contributed with useful discussions. C. C. B. prepared the manuscript with inputs of all authors.

Conflicts of interest

There are no conflicts to declare.

Acknowledgements

C. C. B., A. M. C. and T. D. B. thank Leverhulme Trust Research Project Grant (RPG-2020-005). T. D. B. also thanks the Royal Society for both a University Research Fellowship (URF\R\211013) and a research grant (RGS\R2\212221).

Notes and references

1 H. Furukawa, K. E. Cordova, M. O'Keeffe and O. M. Yaghi, *Science*, 2013, **341**, 1230444.
2 X. Zhao, Y. Wang, D.-S. Li, X. Bu and P. Feng, *Adv. Mater.*, 2018, **30**, 1705189.
3 P. Horcajada, R. Gref, T. Baati, P. K. Allan, G. Maurin, P. Couvreur, G. Férey, R. E. Morris and C. Serre, *Chem. Rev.*, 2012, **112**, 1232–1268.
4 A. Corma, H. García and F. X. Llabrés i Xamena, *Chem. Rev.*, 2010, **110**, 4606–4655.
5 L. E. Kreno, K. Leong, O. K. Farha, M. Allendorf, R. P. Van Duyne and J. T. Hupp, *Chem. Rev.*, 2012, **112**, 1105–1125.
6 I. E. Collings and A. L. Goodwin, *J. Appl. Phys.*, 2019, **126**, 181101.
7 Z. Xiao, H. F. Drake, G. S. Day, J. E. Kuszynski, H. Lin, H. Xie, P. Cai, M. R. Ryder and H.-C. Zhou, *Cell Rep. Phys. Sci.*, 2022, **3**, 101074.
8 E. Fernandez-Bartolome, A. Martinez-Martinez, E. Resines-Urien, L. Piñeiro-Lopez and J. S. Costa, *Coord. Chem. Rev.*, 2022, **452**, 214281.
9 G. Mínguez Espallargas and E. Coronado, *Chem. Soc. Rev.*, 2018, **47**, 533–557.
10 A. Schneemann, V. Bon, I. Schwedler, I. Senkovska, S. Kaskel and R. A. Fischer, *Chem. Soc. Rev.*, 2014, **43**, 6062–6096.
11 C. Healy, K. M. Patil, B. H. Wilson, L. Hermanspahn, N. C. Harvey-Reid, B. I. Howard, C. Kleinjan, J. Kolien, F. Payet, S. G. Telfer, P. E. Kruger and T. D. Bennett, *Coord. Chem. Rev.*, 2020, **419**, 213388.
12 T. D. Bennett and S. Horike, *Nat. Rev. Mater.*, 2018, **3**, 431–440.
13 N. Ma and S. Horike, *Chem. Rev.*, 2022, **122**, 4163–4203.
14 J. Ding, Y. Tang, S. Zheng, S. Zhang, H. Xue, Q. Kong and H. Pang, *Nano Res.*, 2022, **15**, 6793–6818.
15 K.-Y. Zou and Z.-X. Li, *Chem. – Eur. J.*, 2018, **24**, 6506–6518.
16 S. Yang, L. Peng, S. Bulut and W. L. Queen, *Chem. – Eur. J.*, 2019, **25**, 2161–2178.
17 X. F. Lu, Y. Fang, D. Luan and X. W. D. Lou, *Nano Lett.*, 2021, **21**, 1555–1565.
18 B. Li, L. Hong, C. Jing, X. Yue, H. Huang, Q. Jiang and J. Tang, *Microporous Mesoporous Mater.*, 2024, **365**, 112836.
19 Z.-X. Cai, Z.-L. Wang, J. Kim and Y. Yamauchi, *Adv. Mater.*, 2019, **31**, 1804903.
20 B. You, N. Jiang, M. Sheng, W. S. Drisdell, J. Yano and Y. Sun, *ACS Catal.*, 2015, **5**, 7068–7076.
21 X.-C. Xie, K.-J. Huang and X. Wu, *J. Mater. Chem. A*, 2018, **6**, 6754–6771.
22 L. Zhang, H. Bin Wu and X. W. (David) Lou, *J. Am. Chem. Soc.*, 2013, **135**, 10664–10672.
23 L. Zhang, Z. Su, F. Jiang, L. Yang, J. Qian, Y. Zhou, W. Li and M. Hong, *Nanoscale*, 2014, **6**, 6590–6602.
24 A. J. Amali, H. Hoshino, C. Wu, M. Ando and Q. Xu, *Chem. – Eur. J.*, 2014, **20**, 8279–8282.
25 H. Xu, S. Zhou, L. Xiao, H. Wang, S. Li and Q. Yuan, *J. Mater. Chem. C*, 2015, **3**, 291–297.
26 H. Hu, G. Ruan, X. Jiang, H. Pan, Z. Wu and Y. Huang, *New J. Chem.*, 2022, **46**, 8224–8231.
27 X. Li, Q. Sun, J. Liu, B. Xiao, R. Li and X. Sun, *J. Power Sources*, 2016, **302**, 174–179.
28 X. Pan, L. Bai, H. Wang, Q. Wu, H. Wang, S. Liu, B. Xu, X. Shi and H. Liu, *Adv. Mater.*, 2018, **30**, 1800180.
29 X. Li, J. Zhang and W. Li, *J. Ind. Eng. Chem.*, 2016, **44**, 146–154.

30 J. Xu, J. Wang, L. Ge, J. Sun, W. Ma, M. Ren, X. Cai, W. Liu and J. Yao, *J. Colloid Interface Sci.*, 2022, **610**, 98–105.
31 Z. Zhang, Y. Chen, P. Wang, Z. Wang, C. Zuo, W. Chen and T. Ao, *J. Hazard. Mater.*, 2022, **423**, 127103.
32 X.-M. Cao, Z.-J. Sun, S.-Y. Zhao, B. Wang and Z.-B. Han, *Mater. Chem. Front.*, 2018, **2**, 1692–1699.
33 N. Liu, X. Liu and J. Pan, *J. Colloid Interface Sci.*, 2022, **606**, 1364–1373.
34 S. Li, X. Zhang and Y. Huang, *J. Hazard. Mater.*, 2017, **321**, 711–719.
35 S. Cheng, N. Shang, C. Feng, S. Gao, C. Wang and Z. Wang, *Catal. Commun.*, 2017, **89**, 91–95.
36 L. Chang, J. Li, X. Duan and W. Liu, *Electrochim. Acta*, 2015, **176**, 956–964.
37 S. J. Yang, T. Kim, J. H. Im, Y. S. Kim, K. Lee, H. Jung and C. R. Park, *Chem. Mater.*, 2012, **24**, 464–470.
38 S. J. Yang, S. Nam, T. Kim, J. H. Im, H. Jung, J. H. Kang, S. Wi, B. Park and C. R. Park, *J. Am. Chem. Soc.*, 2013, **135**, 7394–7397.
39 M. del Rio, J. C. Grimalt Escarabajal, G. Turnes Palomino and C. Palomino Cabello, *Chem. Eng. J.*, 2022, **428**, 131147.
40 C.-P. Li, Y.-Q. Wu, F.-Y. Zhang, L.-X. Gao, D.-Q. Zhang and Z.-X. An, *Sep. Purif. Technol.*, 2021, **277**, 119618.
41 T. Hussain, P. Nie, B. Hu, X. Shang, J. Yang and J. Liu, *J. Mater. Sci.*, 2021, **56**, 10282–10292.
42 W. Xia, B. Qiu, D. Xia and R. Zou, *Sci. Rep.*, 2013, **3**, 1935.
43 J. Hwang, R. Yan, M. Oschatz and B. V. K. J. Schmidt, *J. Mater. Chem. A*, 2018, **6**, 23521–23530.
44 N. L. Torad, R. R. Salunkhe, Y. Li, H. Hamoudi, M. Imura, Y. Sakka, C.-C. Hu and Y. Yamauchi, *Chem. – Eur. J.*, 2014, **20**, 7895–7900.
45 X. Xu, J. Li, M. Wang, Y. Liu, T. Lu and L. Pan, *ChemElectroChem*, 2016, **3**, 993–998.
46 T. Van Tran, D. T. C. Nguyen, H. T. N. Le, T. T. K. Tu, N. D. Le, K. T. Lim, L. G. Bach and T. D. Nguyen, *J. Environ. Chem. Eng.*, 2019, **7**, 102881.
47 Y. Hou, X.-J. Hu, H.-Y. Tong, Y.-B. Huang and R. Cao, *Inorg. Chem. Commun.*, 2020, **114**, 107825.
48 S. Cheng, N. Shang, X. Zhou, C. Feng, S. Gao, C. Wang and Z. Wang, *New J. Chem.*, 2017, **41**, 9857–9865.
49 W. Jin, H.-J. Li, J. Zou, S. Inguva, Q. Zhang, S. Zeng, G. Xu and X. Zeng, *Mater. Lett.*, 2019, **252**, 211–214.
50 H. J. Lee, S. Choi and M. Oh, *Chem. Commun.*, 2014, **50**, 4492–4495.
51 L. Chen, J. Bai, C. Wang, Y. Pan, M. Scheer and X. You, *Chem. Commun.*, 2008, 1581–1583.
52 X. Zhang, T. Kitao, D. Piga, R. Hongu, S. Bracco, A. Comotti, P. Sozzani and T. Uemura, *Chem. Sci.*, 2020, **11**, 10844–10849.
53 Q. Wang, W. Xia, W. Guo, L. An, D. Xia and R. Zou, *Chem. – Asian J.*, 2013, **8**, 1879–1885.
54 B. Liu, H. Shioyama, T. Akita and Q. Xu, *J. Am. Chem. Soc.*, 2008, **130**, 5390–5391.
55 M. Hu, J. Reboul, S. Furukawa, N. L. Torad, Q. Ji, P. Srinivasu, K. Ariga, S. Kitagawa and Y. Yamauchi, *J. Am. Chem. Soc.*, 2012, **134**, 2864–2867.
56 W. Hu, M. Zheng, B. Xu, Y. Wei, W. Zhu, Q. Li and H. Pang, *J. Mater. Chem. A*, 2021, **9**, 3880–3917.
57 C. Wang, Y. V. Kaneti, Y. Bando, J. Lin, C. Liu, J. Li and Y. Yamauchi, *Mater. Horiz.*, 2018, **5**, 394–407.
58 X. Xu, R. Cao, S. Jeong and J. Cho, *Nano Lett.*, 2012, **12**, 4988–4991.
59 F. Zheng, Y. Yang and Q. Chen, *Nat. Commun.*, 2014, **5**, 5261.
60 R. R. Salunkhe, Y. V. Kaneti and Y. Yamauchi, *ACS Nano*, 2017, **11**, 5293–5308.
61 X. Tan, Y. Wu, X. Lin, A. Zeb, X. Xu, Y. Luo and J. Liu, *Inorg. Chem. Front.*, 2020, **7**, 4939–4955.
62 W. Zhou, Y. Tang, X. Zhang, S. Zhang, H. Xue and H. Pang, *Coord. Chem. Rev.*, 2023, **477**, 214949.
63 Y. Li, Y. Xu, W. Yang, W. Shen, H. Xue and H. Pang, *Small*, 2018, **14**, 1704435.
64 M. Ali, E. Pervaiz, T. Noor, O. Rabi, R. Zahra and M. Yang, *Int. J. Energy Res.*, 2021, **45**, 1190–1226.
65 T.-T. Li, J. Qian and Y.-Q. Zheng, *RSC Adv.*, 2016, **6**, 77358–77365.
66 C. Li, T. Chen, W. Xu, X. Lou, L. Pan, Q. Chen and B. Hu, *J. Mater. Chem. A*, 2015, **3**, 5585–5591.
67 L. Zhang, H. Bin Wu, S. Madhavi, H. H. Hng and X. W. (David) Lou, *J. Am. Chem. Soc.*, 2012, **134**, 17388–17391.
68 T. K. Kim, K. J. Lee, J. Y. Cheon, J. H. Lee, S. H. Joo and H. R. Moon, *J. Am. Chem. Soc.*, 2013, **135**, 8940–8946.
69 F. Zheng, S. Xu, Z. Yin, Y. Zhang and L. Lu, *RSC Adv.*, 2016, **6**, 93532–93538.
70 S. Kong, R. Dai, H. Li, W. Sun and Y. Wang, *ACS Sustainable Chem. Eng.*, 2015, **3**, 1830–1838.
71 Z. Xiu, M. H. Alfaruqi, J. Gim, J. Song, S. Kim, T. V. Thi, P. T. Duong, J. P. Baboo, V. Mathew and J. Kim, *Chem. Commun.*, 2015, **51**, 12274–12277.
72 X. Yang, L. Qiu and X. Luo, *RSC Adv.*, 2018, **8**, 4890–4894.
73 F. Zheng, D. Zhu, X. Shi and Q. Chen, *J. Mater. Chem. A*, 2015, **3**, 2815–2824.
74 C. Castillo-Blas, N. López-Salas, M. C. Gutiérrez, I. Puente-Orench, E. Gutiérrez-Puebla, M. L. Ferrer, M. Á. Monge and F. Gándara, *J. Am. Chem. Soc.*, 2019, **141**, 1766–1774.
75 C. Castillo-Blas, C. Álvarez-Galván, I. Puente-Orench, A. García-Sánchez, F. E. Oropeza, E. Gutiérrez-Puebla, Á. Monge, V. A. de la Peña-O'Shea and F. Gándara, *Nano Res.*, 2021, **14**, 493–500.
76 W. Cho, S. Park and M. Oh, *Chem. Commun.*, 2011, **47**, 4138–4140.
77 H. Pang, B. Guan, W. Sun and Y. Wang, *Electrochim. Acta*, 2016, **213**, 351–357.
78 F. Zhang, L. Hao, L. Zhang and X. Zhang, *Int. J. Electrochem. Sci.*, 2011, **6**, 2943–2954.
79 B. Liu, X. Zhang, H. Shioyama, T. Mukai, T. Sakai and Q. Xu, *J. Power Sources*, 2010, **195**, 857–861.
80 J. Zhao, F. Wang, P. Su, M. Li, J. Chen, Q. Yang and C. Li, *J. Mater. Chem.*, 2012, **22**, 13328–13333.
81 H. Yu, H. Fan, B. Yadian, H. Tan, W. Liu, H. H. Hng, Y. Huang and Q. Yan, *ACS Appl. Mater. Interfaces*, 2015, **7**, 26751–26757.

82 Y. Xia, B. Wang, G. Wang, X. Liu and H. Wang, *ChemElectroChem*, 2016, **3**, 299–308.
83 R. P. Antony, A. K. Satpati, K. Bhattacharyya and B. N. Jagatap, *Adv. Mater. Interfaces*, 2016, **3**, 1600632.
84 Y. Chuan Tan and H. Chun Zeng, *Chem. Commun.*, 2016, **52**, 11591–11594.
85 L. Hu, Y. Huang, F. Zhang and Q. Chen, *Nanoscale*, 2013, **5**, 4186–4190.
86 G. Huang, F. Zhang, L. Zhang, X. Du, J. Wang and L. Wang, *J. Mater. Chem. A*, 2014, **2**, 8048–8053.
87 H. Hu, B. Guan, B. Xia and X. W. (David) Lou, *J. Am. Chem. Soc.*, 2015, **137**, 5590–5595.
88 G. Huang, L. Zhang, F. Zhang and L. Wang, *Nanoscale*, 2014, **6**, 5509–5515.
89 M. Ni, Y. Zhu, C. Guo, D.-L. Chen, J. Ning, Y. Zhong and Y. Hu, *ACS Catal.*, 2023, **13**, 2502–2512.
90 W. Xia, A. Mahmood, R. Zou and Q. Xu, *Energy Environ. Sci.*, 2015, **8**, 1837–1866.
91 K. Shen, X. Chen, J. Chen and Y. Li, *ACS Catal.*, 2016, **6**, 5887–5903.
92 T. Y. Ma, S. Dai, M. Jaroniec and S. Z. Qiao, *J. Am. Chem. Soc.*, 2014, **136**, 13925–13931.
93 R. Das, P. Pachfule, R. Banerjee and P. Poddar, *Nanoscale*, 2012, **4**, 591–599.
94 W. Zhong, H. Liu, C. Bai, S. Liao and Y. Li, *ACS Catal.*, 2015, **5**, 1850–1856.
95 V. P. Santos, T. A. Wezendonk, J. J. D. Jaén, A. I. Dugulan, M. A. Nasalevich, H.-U. Islam, A. Chojecki, S. Sartipi, X. Sun, A. A. Hakeem, A. C. J. Koeken, M. Ruitenbeek, T. Davidian, G. R. Meima, G. Sankar, F. Kapteijn, M. Makkee and J. Gascon, *Nat. Commun.*, 2015, **6**, 6451.
96 X. Wang and Y. Li, *J. Mol. Catal. A: Chem.*, 2016, **420**, 56–65.
97 X. Ma, Y.-X. Zhou, H. Liu, Y. Li and H.-L. Jiang, *Chem. Commun.*, 2016, **52**, 7719–7722.
98 Y.-X. Zhou, Y.-Z. Chen, L. Cao, J. Lu and H.-L. Jiang, *Chem. Commun.*, 2015, **51**, 8292–8295.
99 Y.-Z. Chen, C. Wang, Z.-Y. Wu, Y. Xiong, Q. Xu, S.-H. Yu and H.-L. Jiang, *Adv. Mater.*, 2015, **27**, 5010–5016.
100 J. Long, K. Shen and Y. Li, *ACS Catal.*, 2017, **7**, 275–284.
101 J. Long, Y. Zhou and Y. Li, *Chem. Commun.*, 2015, **51**, 2331–2334.
102 M. Ding, S. Chen, X.-Q. Liu, L.-B. Sun, J. Lu and H.-L. Jiang, *ChemSusChem*, 2017, **10**, 1898–1903.
103 J. López-Cabrelles, J. Romero, G. Abellán, M. Giménez-Marqués, M. Palomino, S. Valencia, F. Rey and G. Mínguez Espallargas, *J. Am. Chem. Soc.*, 2019, **141**, 7173–7180.
104 W. Chen, Y. Zhang, G. Chen, R. Huang, Y. Zhou, Y. Wu, Y. Hu and K. (Ken) Ostrikov, *J. Mater. Chem. A*, 2019, **7**, 3090–3100.
105 C. A. Angell, *Science*, 1995, **267**, 1924–1935.
106 J. Ren, H. W. Langmi, B. C. North and M. Mathe, *Int. J. Energy Res.*, 2015, **39**, 607–620.
107 S. M. Collins, K. E. MacArthur, L. Longley, R. Tovey, M. Benning, C. B. Schönlieb, T. D. Bennett and P. A. Midgley, *APL Mater.*, 2019, **7**, 091111.
108 C. Chakravarty, P. G. Debenedetti and F. H. Stillinger, *J. Chem. Phys.*, 2007, **126**, 204508.
109 S. A. Khrapak, *Phys. Rev. Res.*, 2020, **2**, 12040.
110 A. Seeger, D. Freitag, F. Freidel and G. Luft, *Thermochim. Acta*, 2004, **424**, 175–181.
111 B. K. Shaw, A. R. Hughes, M. Ducamp, S. Moss, A. Debnath, A. F. Sapnik, M. F. Thorne, L. N. McHugh, A. Pugliese, D. S. Keeble, P. Chater, J. M. Bermudez-Garcia, X. Moya, S. K. Saha, D. A. Keen, F.-X. Coudert, F. Blanc and T. D. Bennett, *Nat. Chem.*, 2021, **13**, 778–785.
112 B. K. Shaw, C. Castillo-Blas, M. F. Thorne, M. L. Ríos Gómez, T. Forrest, M. D. Lopez, P. A. Chater, L. N. McHugh, D. A. Keen and T. D. Bennett, *Chem. Sci.*, 2022, **13**, 2033–2042.
113 M. F. Thorne, A. F. Sapnik, L. N. McHugh, A. M. Bumstead, C. Castillo-Blas, D. S. Keeble, M. Diaz Lopez, P. A. Chater, D. A. Keen and T. D. Bennett, *Chem. Commun.*, 2021, **57**, 9272–9275.
114 Y. Zhao, S.-Y. Lee, N. Becknell, O. M. Yaghi and C. A. Angell, *J. Am. Chem. Soc.*, 2016, **138**, 10818–10821.
115 W. Xu, N. Hanikel, K. A. Lomachenko, C. Atzori, A. Lund, H. Lyu, Z. Zhou, C. A. Angell and O. M. Yaghi, *Angew. Chem., Int. Ed.*, 2023, e202300003.
116 V. I. Dimitrov, *J. Non-Cryst. Solids*, 2005, **351**, 2394–2402.
117 P. G. Debenedetti and F. H. Stillinger, *Nature*, 2001, **410**, 259–267.
118 T. D. Bennett, J.-C. Tan, Y. Yue, E. Baxter, C. Ducati, N. J. Terrill, H. H.-M. Yeung, Z. Zhou, W. Chen, S. Henke, A. K. Cheetham and G. N. Greaves, *Nat. Commun.*, 2015, **6**, 8079.
119 K. S. Park, Z. Ni, A. P. Côté, J. Y. Choi, R. Huang, F. J. Uribe-Romo, H. K. Chae, M. O'Keeffe and O. M. Yaghi, *Proc. Natl. Acad. Sci. U. S. A.*, 2006, **103**, 10186–10191.
120 T. D. Bennett, A. L. Goodwin, M. T. Dove, D. A. Keen, M. G. Tucker, E. R. Barney, A. K. Soper, E. G. Bithell, J.-C. Tan and A. K. Cheetham, *Phys. Rev. Lett.*, 2010, **104**, 115503.
121 T. D. Bennett, Y. Yue, P. Li, A. Qiao, H. Tao, N. G. Greaves, T. Richards, G. I. Lampronti, S. A. T. Redfern, F. Blanc, O. K. Farha, J. T. Hupp, A. K. Cheetham and D. A. Keen, *J. Am. Chem. Soc.*, 2016, **138**, 3484–3492.
122 A. M. Bumstead, M. F. Thorne, A. F. Sapnik, C. Castillo-Blas, G. I. Lampronti and T. D. Bennett, *Dalton Trans.*, 2022, **51**, 13636–13645.
123 L. Frentzel-Beyme, M. Kloß, P. Kolodzeiski, R. Pallach and S. Henke, *J. Am. Chem. Soc.*, 2019, **141**, 12362–12371.
124 M. L. Ríos Gómez, G. I. Lampronti, Y. Yang, J. C. Mauro and T. D. Bennett, *Dalton Trans.*, 2020, **49**, 850–857.
125 A. M. Bumstead, I. Pakamorė, K. D. Richards, M. F. Thorne, S. S. Boyadjieva, C. Castillo-Blas, L. N. McHugh, A. F. Sapnik, D. S. Keeble, D. A. Keen, R. C. Evans, R. S. Forgan and T. D. Bennett, *Chem. Mater.*, 2022, **34**, 2187–2196.
126 A. M. Bumstead, C. Castillo-Blas, I. Pakamorė, M. F. Thorne, A. F. Sapnik, A. M. Chester, G. Robertson,

D. J. M. Irving, P. A. Chater, D. A. Keen, R. S. Forgan and T. D. Bennett, *Chem. Commun.*, 2023, **59**, 732–735.
127 J. Song, L. Frentzel-Beyme, R. Pallach, P. Kolodzeiski, A. Koutsianos, W.-L. Xue, R. Schmid and S. Henke, *J. Am. Chem. Soc.*, 2023, **145**, 9273–9284.
128 S. J. Rettig, A. Storr, D. A. Summers, R. C. Thompson and J. Trotter, *J. Am. Chem. Soc.*, 1997, **119**, 8675–8680.
129 L. León-Alcaide, R. S. Christensen, D. A. Keen, J. L. Jordá, I. Brotons-Alcázar, A. Forment-Aliaga and G. Mínguez Espallargas, *J. Am. Chem. Soc.*, 2023, **145**, 11258–11264.
130 Y.-S. Wei, Z. Fan, C. Luo and S. Horike, *Nat. Synth.*, 2024, **3**, 214–223.
131 Z. Fan, Y.-S. Wei, C. Das, K. Kanamori, H. Yamada, K. Ohara and S. Horike, *Chem. Commun.*, 2023, **59**, 14317–14320.
132 L. N. McHugh and T. D. Bennett, *J. Mater. Chem. A*, 2022, **10**, 19552–19559.
133 Y. Wang, H. Jin, Q. Ma, K. Mo, H. Mao, A. Feldhoff, X. Cao, Y. Li, F. Pan and Z. Jiang, *Angew. Chem., Int. Ed.*, 2020, **132**, 4395–4399.
134 Z. Yang, Y. Belmabkhout, L. N. McHugh, D. Ao, Y. Sun, S. Li, Z. Qiao, T. D. Bennett, M. D. Guiver and C. Zhong, *Nat. Mater.*, 2023, **22**, 888–894.
135 S. Li, S. Yu, S. M. Collins, D. N. Johnstone, C. W. Ashling, A. F. Sapnik, P. A. Chater, D. S. Keeble, L. N. McHugh, P. A. Midgley, D. A. Keen and T. D. Bennett, *Chem. Sci.*, 2020, **11**, 9910–9918.
136 C. W. Ashling, D. N. Johnstone, R. N. Widmer, J. Hou, S. M. Collins, A. F. Sapnik, A. M. Bumstead, P. A. Midgley, P. A. Chater, D. A. Keen and T. D. Bennett, *J. Am. Chem. Soc.*, 2019, **141**, 15641–15648.
137 O. Smirnova, S. Hwang, R. Sajzew, L. Ge, A. Reupert, V. Nozari, S. Savani, C. Chmelik, M. R. Reithofer, L. Wondraczek, J. Kärger and A. Knebel, *Nat. Mater.*, 2024, **23**, 262–270.
138 M. T. Islam, L. Macri-Pellizzeri, V. Sottile and I. Ahmed, *Biomater. Sci.*, 2021, **9**, 1826–1844.
139 Y. Hirai, T. Nakanishi, Y. Kitagawa, K. Fushimi, T. Seki, H. Ito, H. Fueno, K. Tanaka, T. Satoh and Y. Hasegawa, *Inorg. Chem.*, 2015, **54**, 4364–4370.
140 E. T. Spielberg, E. Edengeiser, B. Mallick, M. Havenith and A.-V. Mudring, *Chem. – Eur. J.*, 2014, **20**, 5338–5345.
141 A. Qiao, H. Tao, M. P. Carson, S. W. Aldrich, L. M. Thirion, T. D. Bennett, J. C. Mauro and Y. Yue, *Opt. Lett.*, 2019, **44**, 1623–1625.
142 M. A. Ali, X. Liu, Y. Li, J. Ren and J. Qiu, *Inorg. Chem.*, 2020, **59**, 8380–8386.
143 C. Ma, N. Li, D. Li, Z. Gu, Z. Qiao and C. Zhong, *J. Membr. Sci.*, 2023, **683**, 121873.
144 Y. Zhang, Y. Wang, H. Xia, P. Gao, Y. Cao, H. Jin and Y. Li, *Chem. Commun.*, 2022, **58**, 9548–9551.
145 L. Frentzel-Beyme, M. Kloß, R. Pallach, S. Salamon, H. Moldenhauer, J. Landers, H. Wende, J. Debus and S. Henke, *J. Mater. Chem. A*, 2019, **7**, 985–990.
146 A. M. Bumstead, M. F. Thorne and T. D. Bennett, *Faraday Discuss.*, 2021, **225**, 210–225.
147 J. Hou, M. L. Ríos Gómez, A. Krajnc, A. McCaul, S. Li, A. M. Bumstead, A. F. Sapnik, Z. Deng, R. Lin, P. A. Chater, D. S. Keeble, D. A. Keen, D. Appadoo, B. Chan, V. Chen, G. Mali and T. D. Bennett, *J. Am. Chem. Soc.*, 2020, **142**, 3880–3890.
148 C. Das, T. Ogawa and S. Horike, *Chem. Commun.*, 2020, **56**, 8980–8983.
149 S. S. Nagarkar, H. Kurasho, N. T. Duong, Y. Nishiyama, S. Kitagawa and S. Horike, *Chem. Commun.*, 2019, **55**, 5455–5458.
150 T. D. Bennett, D. A. Keen, J.-C. Tan, E. R. Barney, A. L. Goodwin and A. K. Cheetham, *Angew. Chem., Int. Ed.*, 2011, **50**, 3067–3071.
151 S. Park and H.-K. Jeong, *J. Mater. Chem. A*, 2022, **10**, 4992–4998.
152 Y. Feng, M.-Y. Zou, H.-C. Hu, W.-H. Li, S.-L. Cai, W.-G. Zhang and S.-R. Zheng, *Chem. Commun.*, 2022, **58**, 5013–5016.
153 M. F. Thorne, C. Castillo-Blas, L. N. McHugh, A. M. Bumstead, G. Robertson, A. F. Sapnik, C. S. Coates, F. N. Sayed, C. P. Grey, D. A. Keen, M. Etter, I. da Silva, K. Užarević and T. D. Bennett, *Chem. Commun.*, 2022, **58**(11949), 11952.
154 P.-Q. Liao, D.-D. Zhou, A.-X. Zhu, L. Jiang, R.-B. Lin, J.-P. Zhang and X.-M. Chen, *J. Am. Chem. Soc.*, 2012, **134**, 17380–17383.
155 J.-P. Zhang and X.-M. Chen, *J. Am. Chem. Soc.*, 2008, **130**, 6010–6017.
156 X.-N. Cheng, W.-X. Zhang, Y.-Y. Lin, Y.-Z. Zheng and X.-M. Chen, *Adv. Mater.*, 2007, **19**, 1494–1498.
157 S. K. Ghosh, W. Kaneko, D. Kiriya, M. Ohba and S. Kitagawa, *Angew. Chem., Int. Ed.*, 2008, **47**, 8843–8847.
158 A. Kondo, T. Nakagawa, H. Kajiro, A. Chinen, Y. Hattori, F. Okino, T. Ohba, K. Kaneko and H. Kanoh, *Inorg. Chem.*, 2010, **49**, 9247–9252.
159 L. Wen, P. Cheng and W. Lin, *Chem. Commun.*, 2012, **48**, 2846–2848.
160 S. B. Choi, H. Furukawa, H. J. Nam, D.-Y. Jung, Y. H. Jhon, A. Walton, D. Book, M. O'Keeffe, O. M. Yaghi and J. Kim, *Angew. Chem., Int. Ed.*, 2012, **51**, 8791–8795.
161 M. C. Das and P. K. Bharadwaj, *Chem. – Eur. J.*, 2010, **16**, 5070–5077.
162 X.-D. Chen, X.-H. Zhao, M. Chen and M. Du, *Chem. – Eur. J.*, 2009, **15**, 12974–12977.
163 J.-P. Zhang, Y.-Y. Lin, W.-X. Zhang and X.-M. Chen, *J. Am. Chem. Soc.*, 2005, **127**, 14162–14163.
164 M. de J. Velásquez-Hernández, V. B. López-Cervantes, E. Martínez-Ahumada, M. Tu, U. Hernández-Balderas, D. Martínez-Otero, D. R. Williams, V. Martis, E. Sánchez-González, J.-S. Chang, J. S. Lee, J. Balmaseda, R. Ameloot, I. A. Ibarra and V. Jancik, *Chem. Mater.*, 2022, **34**, 669–677.
165 C.-B. Tian, R.-P. Chen, C. He, W.-J. Li, Q. Wei, X.-D. Zhang and S.-W. Du, *Chem. Commun.*, 2014, **50**, 1915–1917.
166 Y. Sakata, S. Furukawa, M. Kondo, K. Hirai, N. Horike, Y. Takashima, H. Uehara, N. Louvain, M. Meilikhov,

T. Tsuruoka, S. Isoda, W. Kosaka, O. Sakata and S. Kitagawa, *Science*, 2013, **339**, 193–196.
167 Z. Hu, C. Tao, H. Liu, X. Zou, H. Zhu and J. Wang, *J. Mater. Chem. A*, 2014, **2**, 14222–14227.
168 H. Chen, Z. You, X. Wang, Q. Qiu, Y. Ying and Y. Wang, *Chem. Eng. J.*, 2022, **446**, 137098.
169 B. Manna, A. K. Chaudhari, B. Joarder, A. Karmakar and S. K. Ghosh, *Angew. Chem., Int. Ed.*, 2013, **52**, 998–1002.
170 R. Guo, Y. Liu, Z. Wang, H. Wang and H. Liu, *CrystEngComm*, 2023, **25**, 4157–4166.
171 V. A. Drebushchak, *J. Therm. Anal. Calorim.*, 2020, **142**, 1097–1113.
172 S. R. G. Balestra, R. Bueno-Perez, S. Hamad, D. Dubbeldam, A. R. Ruiz-Salvador and S. Calero, *Chem. Mater.*, 2016, **28**, 8296–8304.
173 N. Lock, Y. Wu, M. Christensen, L. J. Cameron, V. K. Peterson, A. J. Bridgeman, C. J. Kepert and B. B. Iversen, *J. Phys. Chem. C*, 2010, **114**, 16181–16186.
174 D. Dubbeldam, K. S. Walton, D. E. Ellis and R. Q. Snurr, *Angew. Chem., Int. Ed.*, 2007, **46**, 4496–4499.
175 Y. Wu, A. Kobayashi, G. J. Halder, V. K. Peterson, K. W. Chapman, N. Lock, P. D. Southon and C. J. Kepert, *Angew. Chem., Int. Ed.*, 2008, **47**, 8929–8932.
176 J. D. Evans, J. P. Dürholt, S. Kaskel and R. Schmid, *J. Mater. Chem. A*, 2019, **7**, 24019–24026.
177 L. D. DeVries, P. M. Barron, E. P. Hurley, C. Hu and W. Choe, *J. Am. Chem. Soc.*, 2011, **133**, 14848–14851.
178 I. Grobler, V. J. Smith, P. M. Bhatt, S. A. Herbert and L. J. Barbour, *J. Am. Chem. Soc.*, 2013, **135**, 6411–6414.
179 B. Garai, V. Bon, A. Efimova, M. Gerlach, I. Senkovska and S. Kaskel, *J. Mater. Chem. A*, 2020, **8**, 20420–20428.
180 S. Kitagawa, R. Kitaura and S. Noro, *Angew. Chem., Int. Ed.*, 2004, **43**, 2334–2375.
181 A. Demessence and J. R. Long, *Chem. – Eur. J.*, 2010, **16**, 5902–5908.
182 J. Xiao, Y. Wu, M. Li, B.-Y. Liu, X.-C. Huang and D. Li, *Chem. – Eur. J.*, 2013, **19**, 1891–1895.
183 H. J. Choi, M. Dincă and J. R. Long, *J. Am. Chem. Soc.*, 2008, **130**, 7848–7850.
184 P. L. Llewellyn, S. Bourrelly, C. Serre, Y. Filinchuk and G. Férey, *Angew. Chem., Int. Ed.*, 2006, **45**, 7751–7754.
185 C. Serre, C. Mellot-Draznieks, S. Surblé, N. Audebrand, Y. Filinchuk and G. Férey, *Science*, 2007, **315**, 1828–1831.
186 K. Biradha, Y. Hongo and M. Fujita, *Angew. Chem., Int. Ed.*, 2002, **41**, 3395–3398.
187 M.-H. Zeng, X.-L. Feng and X.-M. Chen, *Dalton Trans.*, 2004, 2217–2223.
188 S. Yang, X. Lin, W. Lewis, M. Suyetin, E. Bichoutskaia, J. E. Parker, C. C. Tang, D. R. Allan, P. J. Rizkallah, P. Hubberstey, N. R. Champness, K. Mark Thomas, A. J. Blake and M. Schröder, *Nat. Mater.*, 2012, **11**, 710–716.
189 E. Y. Lee and M. P. Suh, *Angew. Chem., Int. Ed.*, 2004, **43**, 2798–2801.
190 L. Xiang, D. Liu, H. Jin, L.-W. Xu, C. Wang, S. Xu, Y. Pan and Y. Li, *Mater. Horiz.*, 2020, **7**, 223–228.
191 C. S. Smoljan, Z. Li, H. Xie, C. J. Setter, K. B. Idrees, F. A. Son, F. Formalik, S. Shafaie, T. Islamoglu, L. K. Macreadie, R. Q. Snurr and O. K. Farha, *J. Am. Chem. Soc.*, 2023, **145**, 6434–6441.
192 M. Wriedt, A. A. Yakovenko, G. J. Halder, A. V. Prosvirin, K. R. Dunbar and H.-C. Zhou, *J. Am. Chem. Soc.*, 2013, **135**, 4040–4050.
193 Y. Han, M. A. Sinnwell, S. J. Teat, M. L. Sushko, M. E. Bowden, Q. R. S. Miller, H. T. Schaef, L. Liu, Z. Nie, J. Liu and P. K. Thallapally, *Adv. Sci.*, 2019, **6**, 1802056.
194 D. Liu, T.-F. Liu, Y.-P. Chen, L. Zou, D. Feng, K. Wang, Q. Zhang, S. Yuan, C. Zhong and H.-C. Zhou, *J. Am. Chem. Soc.*, 2015, **137**, 7740–7746.
195 C. Castillo-Blas, V. A. de la Peña-O'Shea, I. Puente-Orench, J. Romerode Paz, R. Sáez-Puche, E. Gutiérrez-Puebla, F. Gándara and Á. Monge, *Sci. Adv.*, 2017, **3**, e1700773.
196 K. Gedrich, I. Senkovska, I. A. Baburin, U. Mueller, O. Trapp and S. Kaskel, *Inorg. Chem.*, 2010, **49**, 4440–4446.
197 I. A. Lázaro, *Eur. J. Inorg. Chem.*, 2020, 4284–4294.
198 J. B. James and Y. S. Lin, *J. Phys. Chem. C*, 2016, **120**, 14015–14026.
199 H. J. Höhne, G. W. H. Hemminger and W. F. Flammersheim, *Differential Scanning Calorimetry*, Springer, 2nd edn, 2003.
200 Q. Zheng, Y. Zhang, M. Montazerian, O. Gulbiten, J. C. Mauro, E. D. Zanotto and Y. Yue, *Chem. Rev.*, 2019, **119**, 7848–7939.
201 F. Gándara and T. D. Bennett, *IUCrJ*, 2014, **1**, 563–570.
202 J. H. Cavka, S. Jakobsen, U. Olsbye, N. Guillou, C. Lamberti, S. Bordiga and K. P. Lillerud, *J. Am. Chem. Soc.*, 2008, **130**, 13850–13851.
203 F. Gándara, F. J. Uribe-Romo, D. K. Britt, H. Furukawa, L. Lei, R. Cheng, X. Duan, M. O'Keeffe and O. M. Yaghi, *Chem. – Eur. J.*, 2012, **18**, 10595–10601.
204 R. N. Widmer, G. I. Lampronti, S. Chibani, C. W. Wilson, S. Anzellini, S. Farsang, A. K. Kleppe, N. P. M. Casati, S. G. MacLeod, S. A. T. Redfern, F.-X. Coudert and T. D. Bennett, *J. Am. Chem. Soc.*, 2019, **141**, 9330–9337.
205 C. Castillo-Blas, J. M. Moreno, I. Romero-Muñiz and A. E. Platero-Prats, *Nanoscale*, 2020, **12**, 15577–15587.
206 C. Castillo-Blas, A. M. Chester, R. P. Cosquer, A. F. Sapnik, L. Corti, R. Sajzew, B. Poletto-Rodrigues, G. P. Robertson, D. J. M. Irving, L. N. McHugh, L. Wondraczek, F. Blanc, D. A. Keen and T. D. Bennett, *J. Am. Chem. Soc.*, 2023, **145**, 22913–22924.
207 A. M. Chester, C. Castillo-Blas, R. Sajzew, B. P. Rodrigues, R. Mas-Balleste, A. Moya, J. E. Snelson, S. M. Collins, A. F. Sapnik, G. P. Robertson, D. J. M. Irving, L. Wondraczek, D. A. Keen and T. D. Bennett, *Chem. Sci.*, 2023, **14**, 11737–11748.
208 A. E. Platero-Prats, A. Mavrandonakis, L. C. Gallington, Y. Liu, J. T. Hupp, O. K. Farha, C. J. Cramer and K. W. Chapman, *J. Am. Chem. Soc.*, 2016, **138**, 4178–4185.
209 M. Mazaj, G. Mali, M. Rangus, E. Žunkovič, V. Kaučič and N. Zabukovec Logar, *J. Phys. Chem. C*, 2013, **117**, 7552–7564.

210 X. Gong, K. Gnanasekaran, Z. Chen, L. Robison, M. C. Wasson, K. C. Bentz, S. M. Cohen, O. K. Farha and N. C. Gianneschi, *J. Am. Chem. Soc.*, 2020, **142**, 17224–17235.
211 Z. Lyu, L. Yao, W. Chen, F. C. Kalutantirige and Q. Chen, *Chem. Rev.*, 2023, **123**(7), 4051–4145.
212 A. Rizvi, J. T. Mulvey, B. P. Carpenter, R. Talosig and J. P. Patterson, *Chem. Rev.*, 2021, **121**, 14232–14280.
213 J. P. Patterson, P. Abellan, M. S. Denny, C. Park, N. D. Browning, S. M. Cohen, J. E. Evans and N. C. Gianneschi, *J. Am. Chem. Soc.*, 2015, **137**, 7322–7328.
214 J. Lyu, X. Gong, S.-J. Lee, K. Gnanasekaran, X. Zhang, M. C. Wasson, X. Wang, P. Bai, X. Guo, N. C. Gianneschi and O. K. Farha, *J. Am. Chem. Soc.*, 2020, **142**, 4609–4615.
215 X. Gong, K. Gnanasekaran, K. Ma, C. J. Forman, X. Wang, S. Su, O. K. Farha and N. C. Gianneschi, *J. Am. Chem. Soc.*, 2022, **144**, 6674–6680.
216 D. Thomas, D. Till and R. Claus, *Science*, 2021, **371**, 371–374.
217 T. Watanabe, S. Keskin, S. Nair and D. S. Sholl, *Phys. Chem. Chem. Phys.*, 2009, **11**, 11389–11394.
218 K. Sillar, A. Hofmann and J. Sauer, *J. Am. Chem. Soc.*, 2009, **131**, 4143–4150.
219 C. L. Hobday, R. J. Marshall, C. F. Murphie, J. Sotelo, T. Richards, D. R. Allan, T. Düren, F.-X. Coudert, R. S. Forgan, C. A. Morrison, S. A. Moggach and T. D. Bennett, *Angew. Chem., Int. Ed.*, 2016, **55**, 2401–2405.
220 M. Ji, X. Lan, Z. Han, C. Hao and J. Qiu, *Inorg. Chem.*, 2012, **51**, 12389–12394.
221 R. Gaillac, P. Pullumbi and F. X. Coudert, *J. Phys. Chem. C*, 2018, **122**, 6730–6736.
222 R. Gaillac, P. Pullumbi, K. A. Beyer, K. W. Chapman, D. A. Keen, T. D. Bennett and F.-X. Coudert, *Nat. Mater.*, 2017, **16**, 1149–1154.
223 R. Gaillac, P. Pullumbi, T. D. Bennett and F.-X. Coudert, *Chem. Mater.*, 2020, **32**, 8004–8011.
224 A. U. Ortiz, A. Boutin, A. H. Fuchs and F.-X. Coudert, *J. Phys. Chem. Lett.*, 2013, **4**, 1861–1865.
225 T. P. Senftle, S. Hong, M. M. Islam, S. B. Kylasa, Y. Zheng, Y. K. Shin, C. Junkermeier, R. Engel-Herbert, M. J. Janik, H. M. Aktulga, T. Verstraelen, A. Grama and A. C. T. van Duin, *npj Comput. Mater.*, 2016, **2**, 15011.
226 N. Castel and F.-X. Coudert, *J. Phys. Chem. C*, 2022, **126**, 19532–19541.
227 A. Duarte Rodrigues, K. Fahsi, X. Dumail, N. Masquelez, A. van der Lee, S. Mallet-Ladeira, R. Sibille, J.-S. Filhol and S. G. Dutremez, *Chem. – Eur. J.*, 2018, **24**, 1586–1605.
228 S. M. J. Rogge, M. Waroquier and V. Van Speybroeck, *Nat. Commun.*, 2019, **10**, 4842.
229 C. Triguero, F.-X. Coudert, A. Boutin, A. H. Fuchs and A. V. Neimark, *J. Phys. Chem. Lett.*, 2011, **2**, 2033–2037.
230 J. Wieme, K. Lejaeghere, G. Kresse and V. Van Speybroeck, *Nat. Commun.*, 2018, **9**, 4899.
231 L. Schaper and R. Schmid, *Commun. Chem.*, 2023, **6**, 233.